Biophysical Techniques to Quantify Tissue Mechanical Forces and Chemical Kinetics

By

Alexander Auner

Dissertation

Submitted to the Faculty of the

Graduate School of Vanderbilt University

in partial fulfillment of the requirements

for the degree of

DOCTOR OF PHILOSOPHY

in

Physics

September 30, 2018

Nashville, Tennessee

Approved:

M. Shane Hutson, Ph.D.

Erin Rericha, Ph.D.

Lisa McCawley, Ph.D.

Richard Haglund, Ph.D.

Dylan Burnette, Ph.D.

To my father, who lit the spark of scientific curiosity in me as a child and inspires me to this day

ACKNOWLEDGMENTS

Lastly, I want to thank my family. Thank you, Tessa, for your love and selfless support during my long hours and for always believing in me. A special thank you to my parents who have always been there for me, providing endless reassurance of my intellectual worth and abilities. I could not have done this without you.

TABLE OF CONTENTS

LIST OF TABLES

LIST OF FIGURES

LIST OF ABBREVIATIONS AND SYMBOLS

AS   Amnioserosa

ATR   Attenuated Total Internal Reflection

CellFit   Cellular Force Inference Toolkit

DMSO   Dimethylsulfoxide

PBS   Phosphate Buffered Saline

f   Internal Polarization (Tension anisotropy)

FTIR   Fourier Transform Infrared Spectroscopy

GB   Germ Band

GFP   Green Fluorescent Protein

Hnt   Hindsight

NA   Numerical aperture

PDMS   Polydimethylsiloxane

PFOA   Perfluorooctanoic Acid

Ret   Retraction Score

RFP   Red Fluorescent Protein

Seg   Segmentation Score

VFM   Video Force Microscopy

β Edge orientation angle

β_0 Angle of minimum tension

γ   Edge tension

θ   Opening angle opposite an edge at a triple junction

Chapter 1

Introduction

This work exemplifies biophysical methods applied to problems in the mechanical forces of tissue development and in chemical binding kinetics. Chapter 1 will provide the necessary background for understanding subsequent chapters. There are three parts to the background: *Drosophila melanogaster* biology, an introduction to soft matter physics and systems biology, and an introduction to lab-on-chip microfluidic devices. This work results from the application of biophysical methods to two different problems: chemical binding kinetics and quantifying mechanical forces in living tissue. Chapter 2 investigates mutation-induced changes to mechanical forces in *Drosophila* embryonic epithelia. Chapter 3 deals with chemical binding in devices used for studying chemical interaction with developing organ systems. This work aims to develop tools and methodologies to analyze cell tension *in-vivo* and chemical binding in microfluidic devices. Each section will discuss past discoveries in physics and biology that motivate the work and provide insight into where the field is heading. The last section of the introduction concludes with an overview and transition to the first of my research chapters.

Drosophila melanogaster as a Model Organism

Drosophila melanogaster (commonly referred to as *Drosophila* and known colloquially as fruit flies) embryos were used primarily to understand how perturbations at the cellular level can affect changes at the tissue level. *Drosophila* is one of the most well-studied organisms in biology for reasons that are both historical and of scientific merit. Fruit flies are inexpensive, easy to care for and have a quick generational turn-over (~2 weeks),

which is particularly useful for genetic crosses. The work in Chapter 2 details a

mathematical model to quantify changes on the tissue level by analyzing changes to cellular

geometry. The purpose of these measurements is to elucidate the mechanical contribution

of intracellular forces to morphogenetic changes during embryo development. The

experimental methods and modelling approach detailed for model systems here is robust

enough to be applied in the future to more complex organisms.

The *Drosophila* genome is well understood[1] and is a popular model organism along with *E.*

coli, C. elegans, S. cerevisae and *D. rerio*. The *Drosophila* genome contains 75% of human

genes related to diseases and further, 100% of the genes in the *Drosophila* genome are

present in humans[1]. *Drosophila* are genetically simple with only four chromosome pairs

and only three being of interest to genetic research (the fourth chromosome is rarely used

for gene insertion and is not influential in development). *Drosophila* sex chromosomes are

similar to humans in that there is one pair and males have an X-Y-chromosome pair, while

females have two X-chromosomes. The entirety of the *Drosophila* genome has been

physically mapped and sequenced and genotypic data is easy to search for in extensive

databases of fly stocks with pre-built mutations.

Genetic variants are widely available and are often combined with catalogued phenotypic

markers on the wings, body or eyes that are easily recognizable under a simple widefield

microscope. Phenotypes are physically observable changes resultant from modification to

an organisms' genome. Phenotypes, such as mechanical changes that disrupt the

epithelium, are created by the insertion of transgenes. More information on *Drosophila*

genetics and the crosses used to create stable stocks is available in Chapter 4. One

prominent phenotypic marker is fluorophore-tagged proteins, which allows imaging of

embryos with a confocal fluorescent microscope. In particular, cell borders can be marked

by tagging green fluorescent protein (GFP) to E-cadherin—a key protein in adherens

junctions that bind epithelial cells[2]. Cadherin proteins can be found in both *Drosophila* and

human epithelial tissue[2].

Our investigative time of interest for biomechanical study is during embryogenesis.

Embryogenesis lasts approximately 24 hours from fertilization and ends with the embryo

transitioning into its larval state. During embryogenesis, fruit flies go through several well

defined temporal stages from a single fertilized cell to a complex multi-cellular organism.

Of interest is the development of the embryonic ectoderm which consists of the outer

epithelial surface made of a single cell layer of tightly adherent cells[3]. The ectoderm is

consists of two tissues—the amnioserosa and the germ band (Figure 1-1).

In animal embryos, large-scale movements of epithelial sheets are necessary for

morphogenetic events[4,5] and wound healing[6,7]. The germ band undergoes mechanical

changes throughout embryogenesis, and this tissue is of particular interest to this work.

This is because genetic perturbations of the germ band have been shown to affect cell

shape and disrupt development[3,8–10]. Changes in germ band mechanics are most noticeable
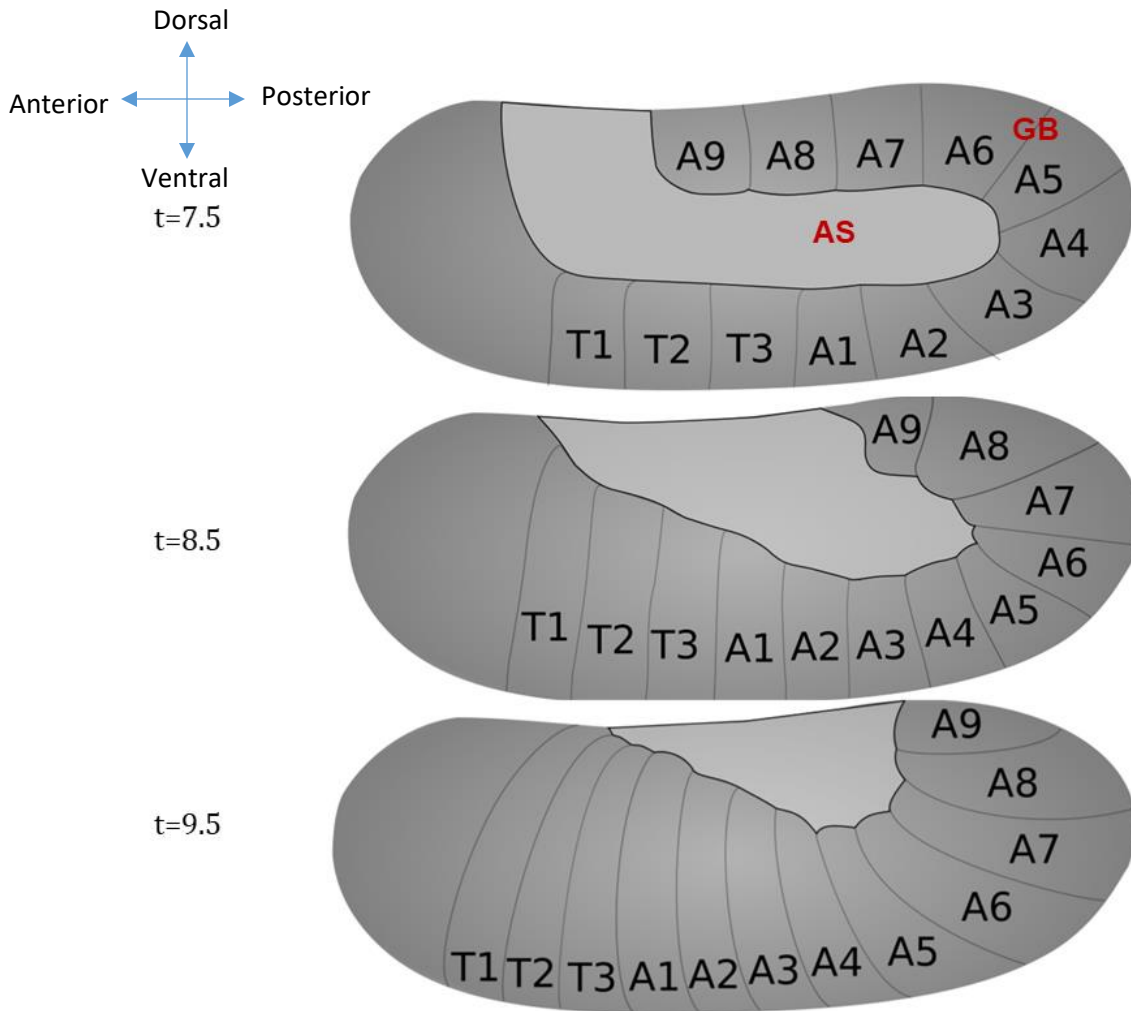
Figure 1-1: Illustration of *Drosophila* embryo undergoing germ band retraction. Germ Band (GB) segments start at the thoracic region T1 and end at A9. The amnioserosa (AS) starts in the U-shaped elongated position.

during germ band retraction where genetic perturbations often result in lethality during that stage[3,8–10]. Germ band retraction takes place 7-8 hours after fertilization and lasts 2-2.5 hours at 25°C[5]. Germ band retraction marks a period of coordinated cell shape change where amnioserosa cells begin in an elongated state at an aspect ratio (ratio of length to width) of up to 11 and end with an aspect ratio of ~1 (isodiametric)[11,12]. On the other hand, the germ band cells elongate throughout retraction[13]. Cell shape change in both tissues results in a change in positioning of the two tissues without cell division or cell

death and with minimal neighbor exchanges (Figure 1-1). Germ band retraction leads into the invagination and subsequent programmed cell death (apoptosis) of the amnioserosa in dorsal closure.

Although the amnioserosa is fated to apoptose during dorsal closure, early apoptosis of the amnioserosa has been shown to be fatal during germ band retraction. In *u-shaped*, *hindsight (hnt)*, *tail-up* and *serpent* mutants, the germ band fails to successfully retract[9]. Each of these mutants deteriorate the amnioserosa to some degree, with all except *tail-up* mutants completely deteriorating the amnioserosa through apoptosis[9]. Of the three, *hindsight* mutants are the phenotypically weakest. Hence, *hindsight* mutants are the closest to wild-type embryos and show evidence of germ band movement taking place at the beginning of retraction resulting in the farthest germ band movement[9]. Regardless, deterioration of the amnioserosa results in a failure of embryo development[8–10]. This has been confirmed physically by ablation of the amnioserosa as well as by expression of *ricin* in amnioserosa, both resulting in retraction failure[10].

Further investigation into *hindsight* mutants have led to attempts to rescue germ band retraction. However, germ band retraction still fails when the amnioserosa is rescued by an H99 Deficiency double-mutant that eliminates caspase-III dependent apoptosis[8]. Further, retraction was partially rescued in *hindsight* mutants with the amnioserosa absent by the overexpression of the insulin receptor gene[8]. This has led to the conclusion that the role of the amnioserosa during germ band retraction is to signal cell shape changes in the

germ band[7]. However, epithelial mechanical properties in *hindsight* mutants remain unassessed. It is possible that a change in germ band mechanical properties could have resulted in the deficiency double-mutant failing and the partial rescue in the insulin receptor overexpression. This work seeks to quantify the internal forces in *hindsight* mutant germ band tissue to assess the role germ band mechanical changes play in development.

Cell tension force within a tissue can be characterized as either active—forces involved in contraction—or passive forces from elastic cellular cytoskeletal connections. One way to determine whether a force exerted internally to a tissue is active or passive is to knock down a gene upstream of the genetic sequence that translates to a contractile molecule that plays a key role in active cell tension such as Myosin II[3]. Rho A is upstream of Myosin II and when Rho A is knocked down in the amnioserosa, germ band retraction is disrupted, showing that amnioserosa cells are actively changing shape[3]. When Rho A was knocked down in germ band cells on the leading edge between the two tissues there was no effect to germ band retraction indicating passive cell shape change[3]. In order to understand the biological significance of quantifying forces that contribute to cell shape change in the germ band, we must understand the origin of cell tension forces.

Soft Matter Physics and Systems Biology

Soft matter physics is a sub-field of condensed matter physics that studies materials that are structurally altered by thermal or mechanical stress. Active soft matter materials convert chemical energy into kinetic energy or mechanical forces. Cells in *Drosophila*

ectoderm can be understood as a non-linear viscoelastic material and the reasons for this

and how cell mechanics can be quantified will be outlined here.   The ectoderm in

Drosophila is constrained apically by the overlying vitelline membrane and basally by the

underlying yolk sac[14]. Additionally, epithelial cells' cytoplasm is virtually incompressible

which allows them to maintain a constant volume throughout embryogenesis[15].

Epithelial cells can withstand compressive forces and generate force on one another from

their cytoskeletal structure. When an epithelial cell deforms, it transfers tension forces

across the entire tissue, directed *in-plane* with the epithelium[16,17]. Through this action, a

single cell can bring about large scale deformation[13,17,18].   The cytoskeletal architecture

consists of two types of filaments: microtubules and actin[19]. Actin is responsible for—

among other things—cell movement and shape change[20,21]. Actin is made of monomer

subunits that bind to each other to form long filaments and also contain sites for cross-

linking proteins which affect filament stability. The actin architecture promotes cell

movement and shape change through the ability to actively assemble and disassemble

filaments[22]. The actin cytoskeleton maintains tension between cells within the ectoderm

by anchor points to adherens junctions[21]. Microtubules are highly dynamic tubulin

polymers and their organization in *Drosophila* epithelium is determined by cell shape[23].

Unlike actin which actively changes to modulate cell tension, microtubules in epithelial

cells provide transport to signaling molecules, some of which affect the actin architecture[23].

The alignment of microtubules are affected by cell shape which then in turn can affect

signaling[23]. Through internal signaling facilitated by microtubules cytoskeleton can adapt

to changes in the surrounding environment such as responding to the hardness of the cell substrate[24,25]. In vertebrates, a third type of filament called intermediate filaments are present throughout the cytoplasm in epithelial cells. These filaments facilitate controlled deformation of cells by transitioning into different structures under different levels of external strain[26]. It is still not understood how *Drosophila* epithelial cells are able to respond to tension without an intermediate filament architecture throughout the cytoplasm[19].

The reverse genetic approach to studying developmental defects resulting from environmental stress involves painstaking investigations of the potentially thousands of subtle biomolecular changes that could result in a mechanical change after altering a known gene. Studies of this nature are traditionally accomplished by knocking down potential genes of interest up to several at a time, followed by investigation of phenotypic changes. The disadvantages of knockdowns are the erroneous results (false positives and negatives from off-target gene interaction) and variable gene-silencing efficiency[27]. Instead, the inverse modeling approach involves careful quantification of mechanical changes that lead to defects and can significantly narrow down phenotypic changes that can then be connected back to biomolecular changes. The field of systems biology involves a complementary approach to inverse modeling used in this work. To form a complete picture of a biological event the field of systems biology involves the use forward modeling. A forward model seeks to create an *in-silico* biological systems whose theoretical framework can be tweaked through key parameters to produce physical predictions.

Systems biology consists of a holistic approach to modelling complex systems in an organism instead of the typical reductionist approach. A 3-dimensional model of *Drosophila* epithelial development to predict physical properties would bring full circle the experimental analysis presented in Chapter 2. The advantage of an *in-silico* model of germ band retraction is to better understand the range of tensions that can support retraction and form plausible theories for how mechanical changes from defects can disrupt it[28]. Combining biophysical techniques to a systems biology approach has been used to successfully describe environmental defects such as cleft palate[29] and fetal alcohol syndrome[30–32]. The development of this approach is important since up to 33% of human pregnancies are thought to be caused by external environmental stress[33].

Lab-on-chip Microfluidic Devices

Although *Drosophila* is a model organism used for studying a broad range of phenomenon, fluidic chip technology is attracting significant interest for studying human disease, for therapeutic application and toxicology studies[34]. Cells grown in petri dishes are isolated from their optimal environment in the body[35]. However, multichannel 3D microfluidic cell culture devices are being designed to mimic the structure and function of human organs and organ systems[36–39]. Precise control of cellular environment provides new opportunities for understanding biochemical and mechanical processes in organ development.

One feature of the translation from physiological differences in organoids grown in microphysiological systems to animal models to human models of development is the

problem of comparing very different scales[36]. Dose response from one organ system to another between different species follows a complex allometric power law relationship between mass, surface area, volumetric flow rate, and metabolic rate[36]. The same relationships apply to organoids grown in a lab-on-chip device[36]. In order to investigate the effects of subtle changes in environment to developing organoids, gas intake and nutrition must be precisely controlled. To accomplish this, the substrate must mimic *in-vivo* conditions as closely as possible. Investigation of molecular signaling in response to stress often uses plated cells and the static introduction of culture media and toxicant of interest. This is followed by an assay for signaling molecules of interest. The signaling molecules of interest end up a thousand-fold diluted, resulting in changes in molecular concentrations that are too small to detect. In order to detect small changes in signal
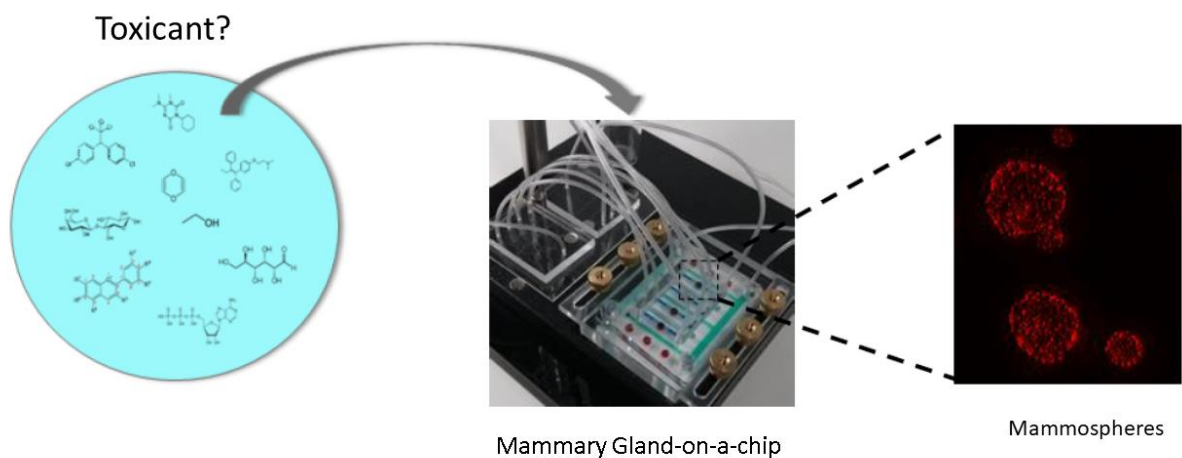
Figure 1-2: A microfluidic device where environmental toxicants are introduced to mammary epithelial cells through channels that lead from a reservoir to a cell chamber filled with collagen matrix. (**Inset**) The cell chamber can be imaged through the device with a wide field fluorescence microscope to observe the cells assembling into mammospheres.

molecules, the volume of media used must be as small as possible in quantity and changed

often. However, frequent changes done manually are both tedious and risk disturbing the

cell environment, resulting in cyclical changes in pH, nutrients and metabolite

concentration. The logical next step is to deliver nutrients and toxicants in a continuous

perfusion as similar as possible to the environment of cells *in-vivo*[34]. Another advantage of

PDMS is its optical transparency, allowing imaging into the perfused sample chamber

without disturbing the specimen (Figure 1-2). Additionally, mechanical forces of interest in

the study of soft matter physics described in the previous section cannot be introduced to

cells in well plates in a realistic manner and require special mechanical sensors[34].

Microfluidic devices can deliver realistic concentration gradients, but in order to accurately

accomplish this the loss of chemical and nutrients to the device itself must be investigated

(Figure 1-3). In order to study a developing organism's response to toxicants, microfluidic
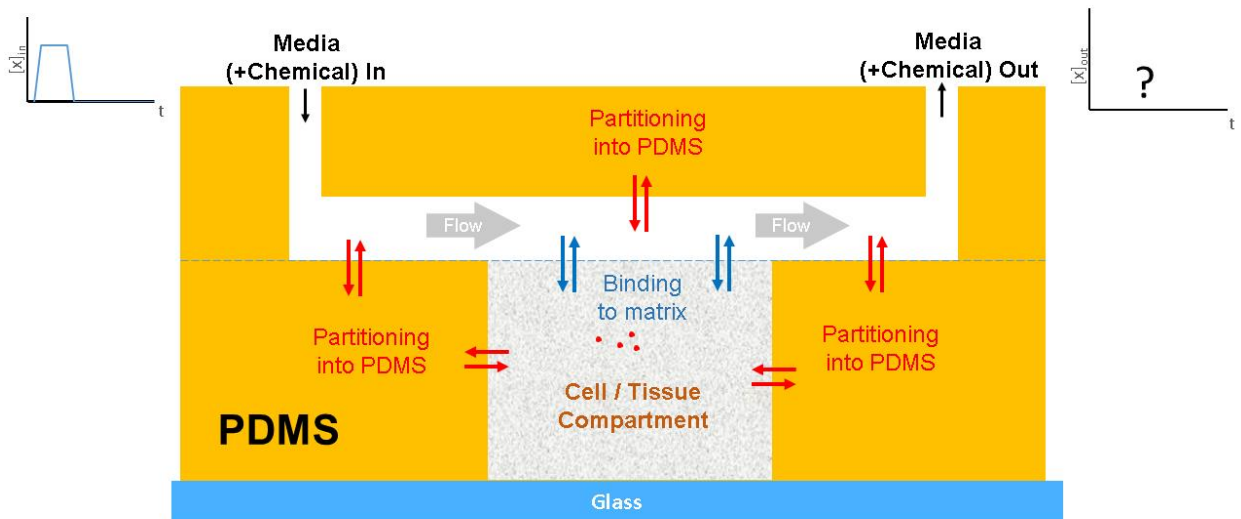
Figure 1-3: Side view of a microfluidic device showing potential loss of chemical and
nutrients to PDMS and collagen matrix.

devices can be interconnected to show complex interplay between organoids. It is imperative that the organoid environment be carefully controlled and environmental stress be quantified. This means any adjustments in exposure need to be accounted for before running the device as shown in Figure 1-3. Some hydrophobic chemicals can bind to the microfluidic channel walls, which are made of a soft, somewhat porous polymer (PDMS). Chapter 3 will go into more detail into a quantitative experiment and model for predicting chemical loss into PDMS.

Overview

This work includes original research on *Drosophila* developmental mechanics (Chapter 2) as well as analysis of microfluidic devices (Chapter 3). Details on the mechanical model of cell-cell interaction is reviewed and applied to a developmental defect due to a genetic mutant. Chapter 3 stands alone as its own research that is necessary to establish an experimental method to investigate toxicology in microfluidic devices. Chapter 4 contains more in-depth explanation of spectroscopic methods, chemical kinetics and *Drosophila* lab work. The final chapter bridges the two major research themes outlining a future direction for developmental toxicology that combines advantages of microfluidic devices and mechanical analysis that can be applied to *Drosophila* and any other organism that allows for imaging of fluorescently tagged cells.

Chapter 2

Analysis of Germ Band Forces in *Hindsight* Mutant Embryos

Abstract

Germ band retraction is a major process in the embryonic development of *Drosophila melanogaster*. During this stage, two tissues in the ectoderm—the germ band and amnioserosa—undergo large scale movement as a single coherent sheet. This movement has been found to result from mechanical forces both internal to the germ band and from external stress from the amnioserosa bringing about changes to cell shape. This work uses a new method of analyzing internal tension in the germ band by measuring relative edge tensions from triple-junction angles. This technique is applied to segments undergoing both normal germ band retraction and in mutant *hindsight* embryos that result in retraction failure due to the early apoptosis of the amnioserosa. It has been hypothesized that germ band cells elongate because of external stress from the amnioserosa and that internal forces to the germ band oppose elongation. In order for germ band cells to elongate from internal polarization in a *hindsight* mutant, the direction of polarization would need to rotate 90°. Nonetheless, our results indicate that absence of the amnioserosa has no measurable effect on the magnitude or direction of the internal polarization in the germ band. Further, in the absence of amnioserosa the germ band moves to fill in the empty space. This intriguing result points to the possibility of another external mechanism driving germ band movement during retraction.

Introduction

This Chapter addresses how to quantify a genetic defect that alters germ band mechanics during embryonic development. Understanding mechanical forces in the germ band is the first step towards recognizing how changes in tension in the ectoderm can modify *Drosophila* embryogenesis leading to a better understanding of large scale movement of epithelial sheets.

Germ band retraction involves the large-scale movement of the germ band and amnioserosa as a single coherent sheet. During retraction the amnioserosa moves to occupy the dorsal surface of the embryo and the germ band retracts to occupy it's final position with end segments occupying the posterior end of the embryo (Figure 1-1)[3]. The molecular initiation of this movement is still not understood, however, the onset of retraction does coincide with a pulse of ecdysone signal in the amnioserosa[40]. Germ band movement during retraction takes place in the absence of cell division and intercalation[3]. Cell division during germ band retraction was investigated in *string* mutants that do not undergo mitosis. In these mutants, retraction was found to occur normally[41]. Further evidence that germ band retraction being a mechanical process comes from dominant negative Rho A mutants that disrupt actomyosin contractility directly resulting in retraction failure[3].

Several genetic mutations can lead to failures of germ band retraction. Among these is hindsight (*hnt*), a gene that codes for a protein with fourteen C_2H_2-type zinc-fingers, that is required in the maintenance of the amnioserosa and that has been hypothesized to exert a

regulatory control on germ band retraction[9,42]. Zinc-fingers are small proteins that require

Zn^{2+} ions in order to stabilize their three-dimensional structure. Zinc-finger proteins are

ubiquitous and 3% of the active human genome codes for them[43]. *hnt* in particular codes

for a zinc-finger transcription factor functioning as a DNA-binding domain and is found in

the nucleus of several tissues prior to and during germ band retraction[42]. Surprisingly, in

the ectoderm, *hnt* is only expressed in the amnioserosa and not the germ band[9]. In the

amnioserosa, *hnt* was found to have a maintenance role. In *hnt* mutants, apoptosis is

initiated early resulting in tissue wide cell death[9]. Apoptosis of the *Drosophila* ectoderm is

initiated when the reaper (*rpr)* gene is turned off resulting in DIAP1—the antiapoptosis

protein—not being transcribed which then results in the disintegration of the cell[44].

During other stages, the *hindsight* transcription factor has been found to regulate ovulation

in ovarian follicles and stem cell differentiation in the adult midgut. The human homolog of

hnt, RREB1, is a transcription factor that regulates the expression of calcitonin in bone

marrow for cell differentiation and has been implicated in the context of cell differentiation

of thyroid carcinoma[45–47].

The germ band retraction stage of *Drosophila* embryogenesis has been well studied from a

cell forces perspective[3,11,12,28]. Understanding the quantitative degree of internal forces in

the germ band will aid in linking genetic perturbations to physical changes that disrupt

development. In particular, germ band retraction involves large scale movement directly

resultant from changes in cell geometry[3,12]. Understanding the link between cell geometry

and tissue-wide tension during this stage allows for a better understanding of the mechanism that causes cell elongation internal to the germ band.

Traditional methods of measuring cell forces often involve invasive experiments such as recoil measurement by means of laser ablation, fluorescence resonance energy transfer (FRET), magnetic cytometry of microinjected ferrous particles or microinjection and optical trapping of microbeads[12,48–51]. Direct techniques of force measurement such as atomic force microscopy or surface tension measurement through aspiration are unavailable for *in-vivo* study of *Drosophila* since surface access is prohibited by the vitelline membrane. Computational models are a great alternative to these methods provided the right constraints on these models are realized. An inverse modelling approach involves fitting a model to experimental data to extract parameters such as cell tension or internal pressure. This approach is particularly useful as it doesn't require the time-consuming step of having to predict morphological outcomes of many combinations of forces. This has resulted in several techniques that rely on finite element methods to calculate the relative tension in cells. The first model to apply this reverse approach to the *Drosophila* germ band is video force microscopy (VFM). VFM calculates forces that must be present in order to drive the motions observed from one temporal frame to the next in a large dataset of cell deformations[52]. Often the problem of force inference techniques such as VFM is that a given dataset can result in an underdetermined system[53]. This was addressed in Bayesian force inference which uses priors to solve underdetermined systems of force equations. The priors were that edge tension and pressure are Gaussian distributed with a mean of

16

one and zero, respectively[53]. As an alternative, CellFit uses the curvature of cell edges and additional pressure balance equations to produce an overdetermined system of equations[53]. The finite element models used in this analysis are simplified by the assumption that junctions where three cell edges come together known as triple junctions are at a quasi-static equilibrium[53]. This assumption is reasonable because imaging of germ band retraction records major cell movement on slow timescales (on the order of hours). This method is still computationally expensive for large numbers of cells for whole germ band comparison over time. Recent work by Lacy *et al.* has resulted in a new method of analysis of internal tissue tension forces known as β-θ analysis[11]. This technique solves for a global polarization relationship between edge tension in different germ band segments, instead of allowing each edge tension to vary independently. This results in a well posed inverse problem.

Germ band failure due to changes in external tension forces from the amnioserosa is well studied[12,28,54]. However, there exist several mutants that disrupt germ band retraction which are not well understood from a mechanical perspective. These mutants provide a good opportunity to investigate whether failure of retraction could be mechanical in nature. In *hnt* mutants, the amnioserosa apoptoses early during germ band retraction leading to failure[8]. Previous investigations have sought to look for a molecular signaling cause of germ band failure in *hindsight* mutants, but none have yet been identified[8]. The drawback of early investigation of *hnt* mutants is that they lack modern *Drosophila* tools such as fluorescent cell border markers that would provide the contrast necessary in germ

17
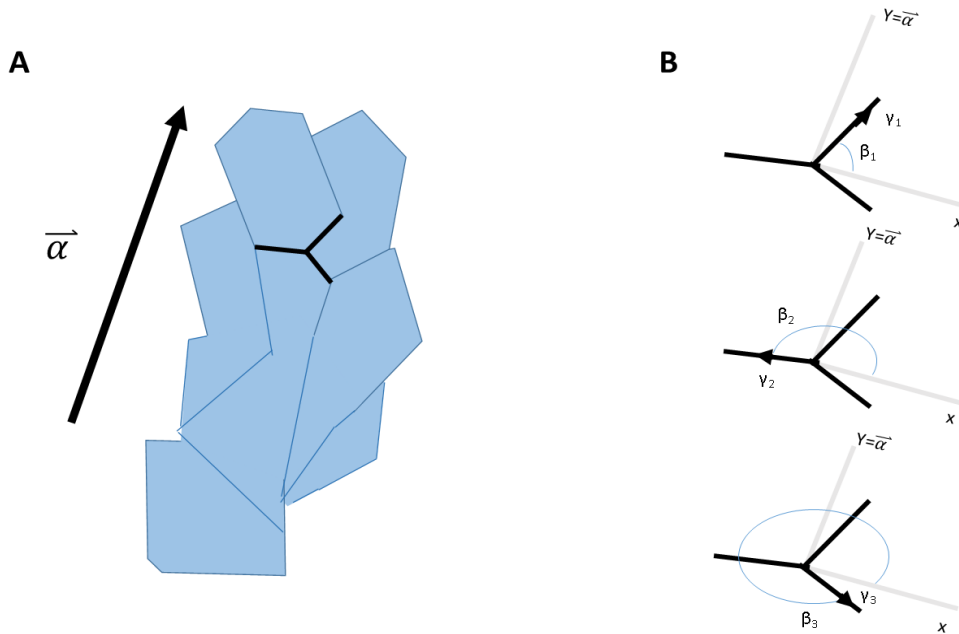
Figure 2-1: (A) An example cell tissue sheet with axis of elongation indicated by vector, $\vec{\alpha}$. (B) A triple junction from the cell sheet with denoted edge tensions γ_i and orientation angles β_i, that are oriented with respect to the x-axis defined as the perpendicular axis to the orientation angle.

band cells to identify structural changes in the mutant[8,9]. In this chapter, I investigate the mechanical structure of the germ band and present novel findings of a quantitative analysis to structural changes in the *hnt* mutant germ band.

β-θ Theory

Lacy *et al.* developed a method known as β-θ analysis that is less computationally taxing and powerful for seeing an overall picture of the tension across germ band segments[11]. The crux of this analysis lies in the assumption that every triple junction between three cells exists in a state of equilibrium. Static equilibrium conditions mean that the net force along any axis at a triple junction is zero. The net force in a junction can be written as the sum of the tension along each edge, $\vec{\gamma_i}$, (where i=1,2,3 for 1st, 2nd and 3rd edge respectively)

$$\vec{F}_{net} = 0 = \sum_{i=1}^{3} \vec{\gamma_i} \qquad (2\text{-}1).$$

The triple junctions in Figure 2-1B also show the force body diagram of edge tension in the junction at equilibrium. Each edge carries tension along its axis, but unlike typical force body problems, the absolute tension is not known for any edge. Fortunately, to understand cell shape change from tension at each junction, only the relative tension, or ratio of tensions, among the three edges in the junction is necessary. More specifically, β-θ analysis measures the degree to which the directional components of average tension are stronger along one axis (tension anisotropy). The tension vector, $\vec{\gamma_i}$, along each edge has a corresponding direction given by orientation angle β_i. The orientation angles shown in Figure 2-1B are defined relative to an x-axis that points perpendicular to the direction of $\vec{\alpha}$, the direction of tissue elongation. Additionally, a special angle can be defined to point to the direction of minimum tension, β_0, shown in both Figures 2-2 and 2-3.

Changes in tension anisotropy in a tissue segment indicates mechanical changes in the cytoskeletal structure of germ band cells. Quantifying anisotropy can indicate whether a change in cell geometry is more from internal or external forces. In order to quantify the anisotropy of a tissue segment, the simplest form for tension that includes a parameter to measure the degree of anisotropy can be considered to have the form

$$\gamma = \bar{\gamma}(1 - \frac{|f|}{2}cos[2(\beta - \beta_0)]) \qquad (2\text{-}2)$$

where $\bar{\gamma}$ is the average edge tension and f is the anisotropy (internal polarization) parameter. The anisotropy parameter varies between 0 ($\gamma = \bar{\gamma}$) and 2 ($\gamma = 0\ to\ 2\bar{\gamma}$).

Combining equations 2-1 and 2-2, the total force along the x and y-axis can be written

$$F_{net,x} = 0 = \sum_{i=1}^{3} \gamma_i cos\beta_i$$

$$F_{net,x} = \sum_{i=1}^{3} \bar{\gamma}\left[1 - \frac{|f|}{2}cos2(\beta - \beta_0)\right]cos\beta_i \qquad (2\text{-}3a);$$
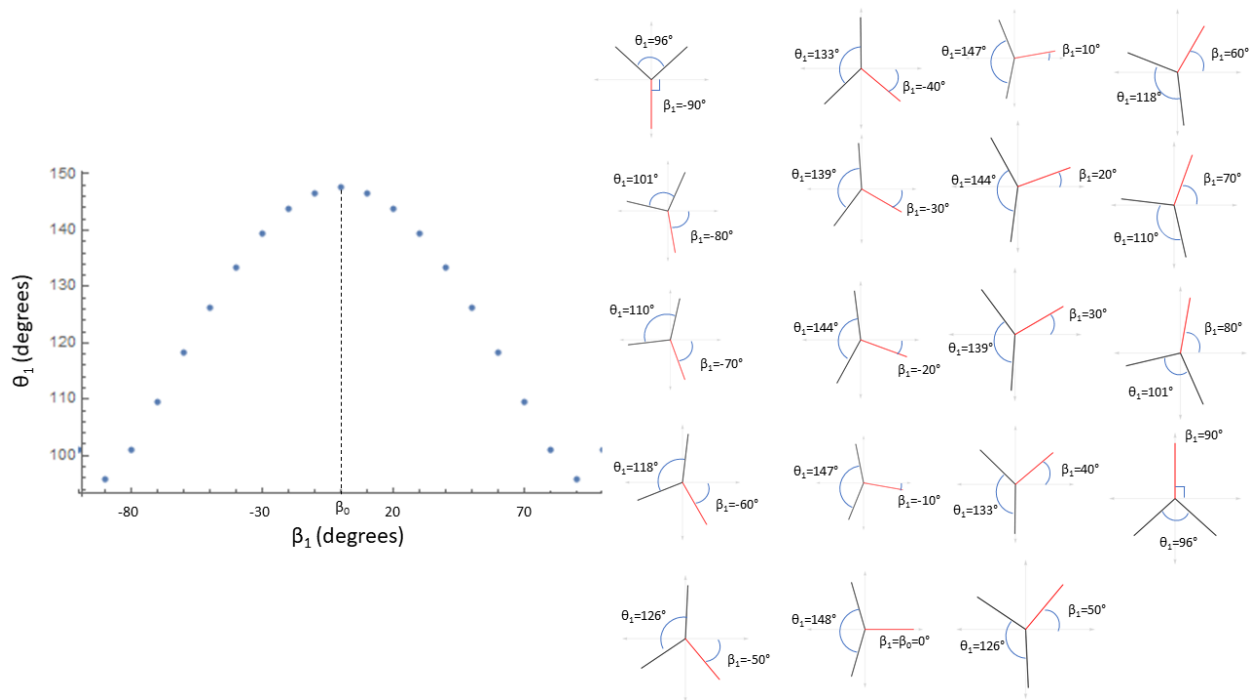
Figure 2-2: (A) β-θ plot for an f value of 0.6. β_0 is indicated by dashed line at 0 degrees. (B) Unique triple junction angles for a given β_1 from -90 to 90 degrees in steps of 10 degrees that correspond to the β-θ plot. Note that here the direction of β_0 is marked by the positive x-axis.

$$F_{net,y} = 0 = \sum_{i=1}^{3} \gamma_i sin\beta_i$$

$$F_{net,y} = \sum_{i=1}^{3} \bar{\gamma} \left[1 - \frac{|f|}{2} cos2(\beta_i - \beta_0)\right] sin\beta_i \qquad (2\text{-}3b).$$

Using these two equations, the anisotropy parameter (f) can be determined by a fit to combinations of edge orientations present in a tissue. For each anisotropy value (f), Equations 2-3a-b yields unique solutions for theoretical distributions of edge orientation angles shown in Figure 2-2B. It is possible to plot distributions of theoretical edge orientations in a tissue segment because each β_1 has a unique solution for β_2 and β_3 for a given theoretical anisotropy. Rather than specify all three edge orientation angles, analysis can be simplified by replacing β_2 and β_3 with the opening angle opposite β_1 called θ_1 (Figure 2-2B). For a given f value, β_1 and θ_1 combinations can be graphed to create a β-θ plot shown in Figure 2-2A.

After analysis of theoretical plots of θ vs. β, several trends emerge to simplify anisotropy calculations. The first trend is that the direction of minimum tension, β_0, always corresponds to the maximum opening angle. This also means the minimum opening angle (θ_{min}) is opposite the direction of maximum tension, which is 90 degrees from β_0, by definition (Figure 2-2). The opening angle's dependence on tension in the opposite edge can be seen in simulated tension anisotropy of Figure 2-4. As edge tension increases, the opening angle opposite that edge decreases. The second trend is that a greater range of θ_1 in a β-θ plot corresponds to a larger anisotropy (f) value (Figure 2-3). In order to solve the
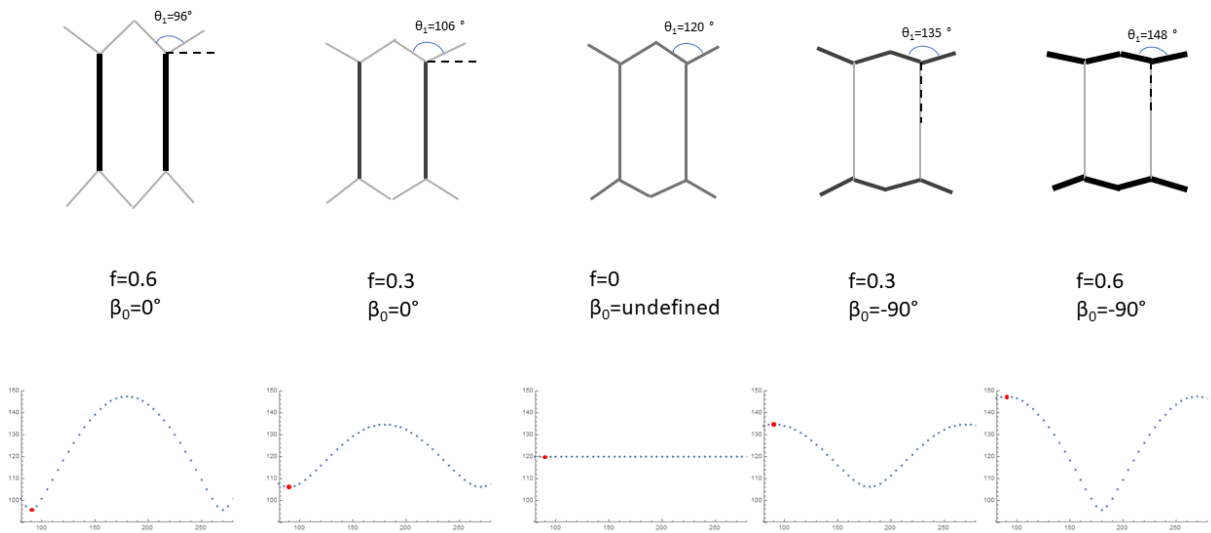
Figure 2-3: (A) Example of one set of edge orientations that yield a given anisotropy with minimum tension oriented along the dashed line and β_1 is the edge fixed at -90°. (B) Range of θ values corresponding to edge orientations across segment that result in the internal polarization depicted in (A). The red dot marks the data point that corresponds to the angles in (A).

inverse problem of finding an anisotropy for a set of known edge orientations, a theoretical β-θ plot is created for f values from 0 to 1.8 in steps of 0.1. From these β-θ plots, an interpolation function is created that maps a combination of edge and opening angle orientations to an f. Through fitting the distribution of angles in triple junctions averaged throughout the tissue segment we can calculate the tension anisotropy.

Triple junction examples in a theoretical segment from a tissue segment that represents data from an experimental measurement are shown in Figure 2-4C. $\vec{\alpha}$ points in the direction of increasing aspect ratio for the segment as a whole; it also happens to be nearly

22

perpendicular to β_0 (dashed line), conveniently allowing β_0 on average to be closely aligned with the x-axis. On its own, internal polarization is contractile and should cause perpendicular elongation (i.e. if minimum tension is defined along β_0, then that is also the direction internal tension would cause elongation); however, the germ band does not exist in isolation and there is also a force contribution from the neighboring amnioserosa's pull across the entire segment (σ_y) and pull from segment boundaries on one another (σ_x) (Figure 2-4B)[12]. The amnioserosa pulls in both directions of σ_y due to the fact that the germ band segments wrap around and make contact on both sides of the amnioserosa. Example edge orientations relative to direction of minimum tension are shown in Figure 2-4. Here the angles are rotated from the illustration orientation to where the axis of elongation is vertical as is done in analysis of experimental data (Figure 2-4). The interpolation
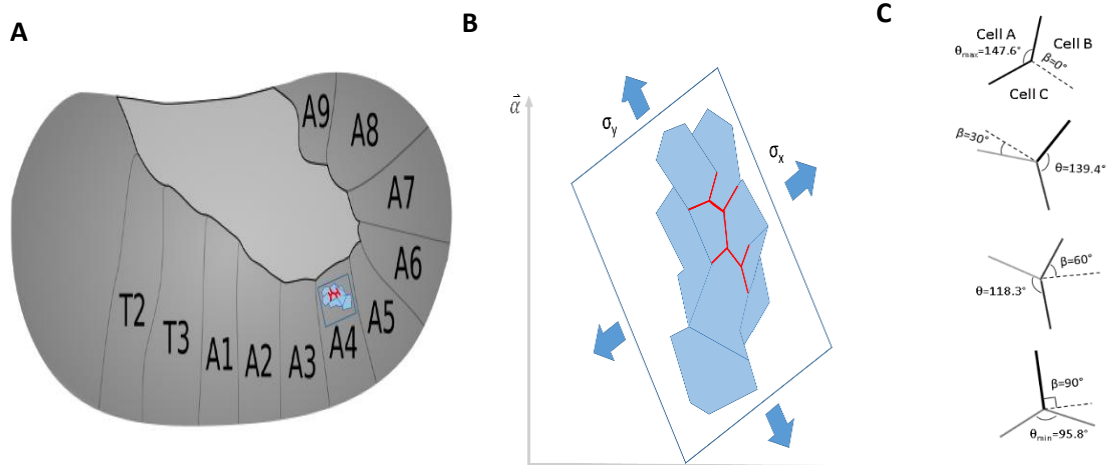
Figure 2-4: (A) Cells of interest in segment A4 are identified with example triple junction edges marked in red (B) Blown up view of cells that compose junctions that has been rotated to align with the vertical axis of elongation (α). The outside arrows represent the external stress (σ) on the entire segment from the amnioserosa. (C) Example combinations of edge orientation angles for marked cells. β_0 is marked by the dashed line. β marks the direction of an edge with its corresponding opening angle θ. The tension of an edge is marked by the edge thickness.

23
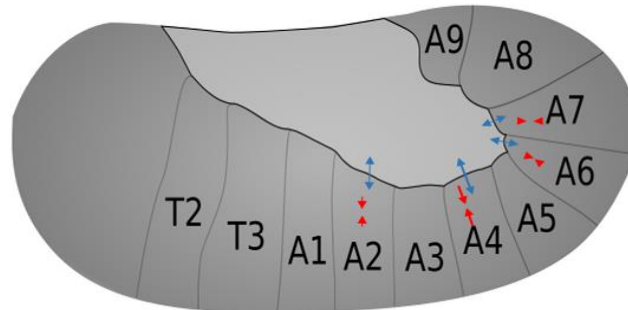
Figure 2-5: Illustration of an embryo in mid-germ band retraction. Arrows for segments A2, A4, A6, and A7 represent the direction and approximate magnitude of maximum internal tension (β_0+90°, red) and axis of elongation (α, blue).

functions are then fit to measured β and θ angles extracted from fluorescent confocal images to determine the internal polarization of the tissue segment.

The resulting picture of the germ band internal polarization is shown in Figure 2-5. The force of contraction in germ band triple junctions aligns with the axis of elongation. The direction and approximate magnitude of maximum tension (β_0 +90°) is shown along with α in Figure 2-5. The axis of elongation for each segment used in β-θ analysis is apparent when compared with the direction of segment elongation in Figure 1-1.

Materials and Methods

Drosophila Stocks

Imaging of normal germ band over time was done with Ubi-DE-Cad-GFP embryos (*Drosophila* Genetic Research Center, Kyoto, Japan). To create male *hnt* mutant embryos, y[1] peb[hnt-E8]/Fm7c mutant stock was crossed with a RFP tagged balancer, Fm7c, P[w[+mC]=2xTb[1]-RFP]FM7c, sn[+]/oc[otd-XC86] (Bloomington *Drosophila* Stock Center, Bloomington, Indiana). Embryos were collected and prepared following previously established protocols for both live imaged embryos for normal germ band retraction or fixed *hnt* embryos[55]. Staining was done with monoclonal anti-α-spectrin (Antibody 3A9, Developmental Studies Hybridoma Bank, University of Iowa), and then with Alexa Fluor 488 donkey anti-mouse IgG (Molecular Probes, Life Technologies, Grand Island, NY).

Imaging

Embryos were imaged with a 40X, 1.3 NA oil-immersion objective on a spinning disk confocal microscope (WaveFX-X1, Quorum Technologies, Ontario, Canada; built onto an Eclipse Ti, Nikon Instruments, Melville, NY). Image stacks (40-70 μm deep with a 1-μm step size) were converted into z-projections consisting of approximately the first 5-μm deep epithelial layer using ImageJ[56]. Multiple frames were then stitched together in ImageJ to create a complete image of the embryo. Cells were segmented using SeedWater Segmenter[57] and then the output cell outlines and triple junction angles were analyzed in Mathematica (Wolfram Research, Champagne, IL)[11].

Results

A single Ecad-GFP embryo was imaged at five-minute intervals for ~2 hours throughout

germ band retraction. The fluorescent images were converted into cell outlines so that

the β-angles could be extracted from each segment. The internal polarization, direction of

minimum tension and aspect ratio were analyzed for four segments in a single embryo for

~1.5 hours of germ band retraction (Figure 2-6). The results show a clear pattern of

increased internal polarization across all segments starting in mid-germ band retraction

and stabilizing at a higher polarization towards the end of retraction. The aspect ratio

roughly doubles for germ band cells across all segments during germ band retraction.

Interestingly, in contrast to predictions by Lynch *et al.*, results from β-θ analysis closely
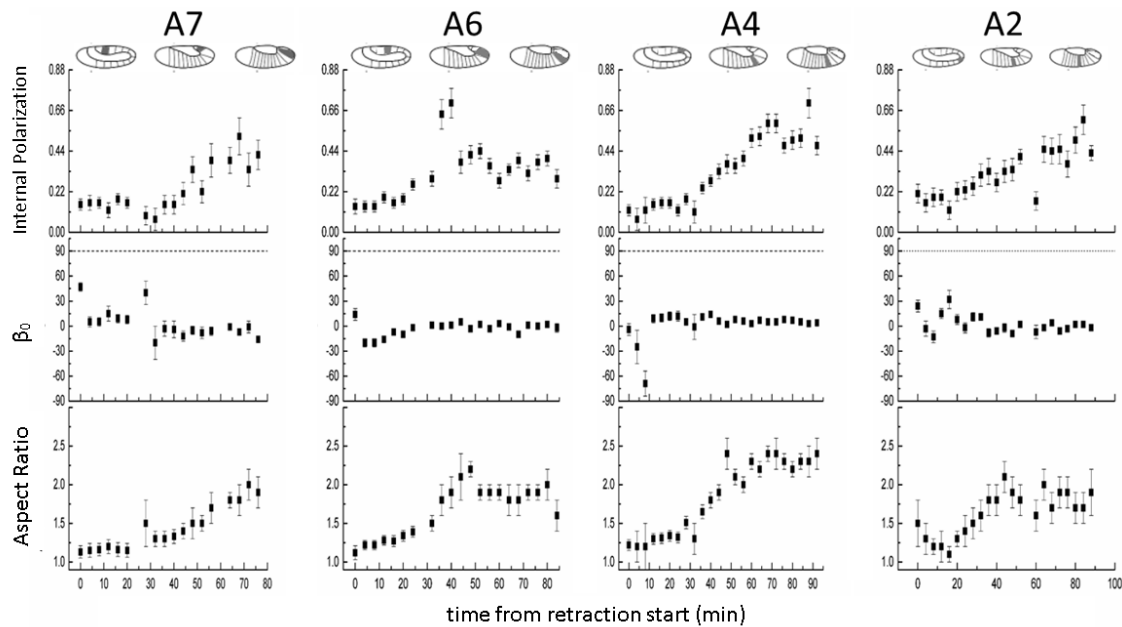
band retraction. Data points are averaged values of 20-40 cells from the tissue segment
indicated at the top. Cartoons illustrate the time period of early, mid and late germ
band retraction. (Top) Internal Polarization over time. (Middle) β-angle over time.
(Bottom) Composite aspect cell ratio over time.

align with Lacy *et al.* results for other segments that the direction of increased polarization is nearly perpendicular to the direction of elongation regardless of segment position[11,12].

Figure 2-7 shows novel confocal fluorescence imaging of the *hnt* mutant germ band in fixed and stained embryos. Some features of *hnt* are clearly identifiable like the absence of the amnioserosa and the altered shape of germ band segments from normal germ band during retraction. The cross to create *hnt* progeny creates both wild-type embryos and *hnt* dominant phenotype males (see Chapter 4). Since it is impossible to identify male embryos from female, before analyzing mutant embryos for mechanical changes, the *hnt* phenotype
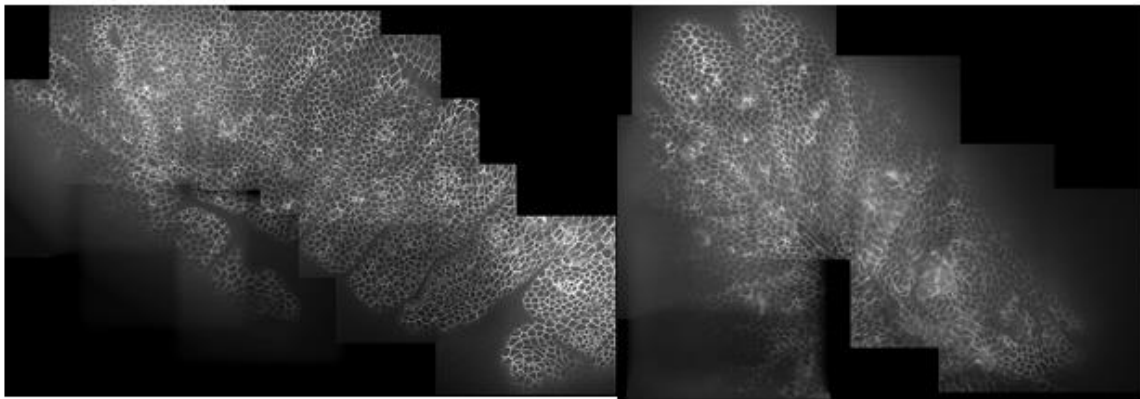
Figure 2-7: Spinning disk confocal images of α-spectrin stained *hindsight* embryos at the time point of mid-germ band retraction (~8.5 hours). The lack of amnioserosa and unusual position of germ band segments shown here characterize the hindsight phenotype.

27

Table 2-1: Frequency and characterization of *hindsight* defect compared to wild-type control embryo

t	$N_{ventral}$	N_{dorsal}	AS Score	Ret Score	Seg Score
9.5	13	31	0: 1/31 1: 3/31 2: 27/31	0: 16/31 1: 9/31 2: 4/31 3: 2/31	0: 1/31 1: 14/31 2: 16/31
10.5	9	15	0: 3/15 1: 4/15 2: 8/15	0: 9/15 1: 2/15 2: 0/15 3: 4/15	0: 4/15 1: 7/15 2: 4/15
11.5	4	33	0: 4/33 1: 6/33 2: 23/33	0: 10/33 1: 1/33 2: 2/33 3: 20/33	0: 3/33 1: 3/33 2: 27/33

AS Score: 0-AS absent, 1-partial AS, 2-AS fully present
Ret Score: Based on Telson position 0-No retraction, 1-50% retracted, 2-Fully Retracted, 3-Dorsal Closure
Seg Score: 0-No segmentation, 1-loosey organized, 2-Full segmentation

Table 2-2: Correlation of AS Score to Ret Score

t=9.5

		Ret Score			
		0	1	2	3
	0	1	0	0	0
AS Score	1	3	0	0	0
	2	12	9	4	2

t=10.5

		Ret Score			
		0	1	2	3
	0	3	0	0	0
AS Score	1	4	0	0	0
	2	2	2	0	4

t=11.5

		Ret Score			
		0	1	2	3
	0	4	0	0	0
AS Score	1	6	0	0	0
	2	0	1	2	20

needs to be characterized from the other progeny of the cross that exhibit a wild-type

phenotype. The results of characterization are shown in Table 2-1 for the three collection

time points taking place after egg laying. The number in the $N_{ventral}$ (unscorable) column

represent samples that were imaged, but due to their orientation were unable to be staged

or characterized. The embryo characterization was dependent on three qualities: the

presence of amnioserosa, degree of retraction, and degree of segmentation. Apoptosis of

the amnioserosa is a hallmark phenotypic marker of *hnt* mutants. Thus, recording the

prevalence of amnioserosa gives a strong impression of the degree of penetrance of *hnt*.

Roughly 27% of scored embryos exhibited partial or fully degraded amnioserosa (Table 2-

1). From the results of the Mendelian genetic cross, the expected prevalence of the *hnt*

genotype is 25%. Retraction score marks the approximate position of the farthest A9

segment (see Figure 1-1). It would be expected that in the absence of the amnioserosa and

knowing germ band retraction will fail before completion, that *hnt* embryos would not have

a full retraction. The prevalence of unretracted germ band is ~44% (Table 2-1). Finally, as

germ band retraction progresses, segmentation becomes more prominent. In the absence

of normal retraction, it is possible segmentation would be less prominent and more closely

resemble the start of retraction or even collapse into disorganization. Of embryos suitable

for characterization, ~41% had loose or no organization of germ band segments (Table 2-

1). These results when taken together indicate that in addition to *hnt* embryos, there is

also the possibility of early wild-type embryos in late germ band extension that have not

yet segmented and retracted due to an uncertainty of ±1 hour for the timing of the embryo

fixation. In order to further characterize hnt penetrance it is necessary to combine the two

29

most quantitative and reliable markers: amnioserosa and retraction scores in Table 2-2.

Here the number of embryos seen with partial or no amnioserosa and also no retraction is

~27% (Table 2-2). From these results, selection of *hnt* embryos for β-θ analysis met the

criterion of a AS score of 0 or 1, a retraction score of 0 and a segmentation score of 1 or 2.

Wild-type embryos were selected for analysis that met the criterion of an AS score of 2,

retraction score of 3 and segmentation score of 2.

The results of β-θ analysis for *hindsight* and wild-type embryos is shown in Figure 2-8.

Unlike Figure 2-6, comparison between segments for wild-type and *hnt* is shown as a

snapshot in time for fixed embryos rather than a live embryo comparison at different

timepoints. The other difference is the time these embryos were fixed. Embryos analyzed

in Figure 2-8 were staged at ~180-240 minutes after the start of germ band retraction.

Because this analysis takes place long after previous germ band data, it does not lend itself

to a strictly direct comparison. The internal polarization of wild-type germ band varies
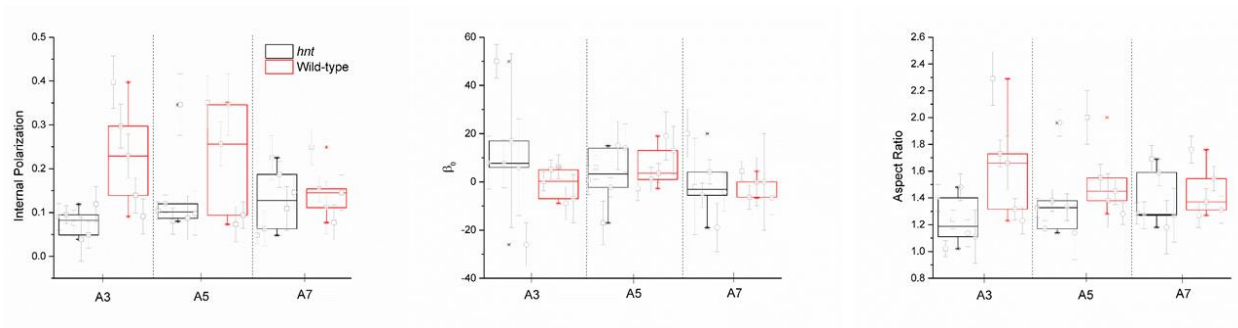
Figure 2-8: Comparison of *hindsight* and wild-type embryos at late germ band retraction for three segments. Values are averaged over >20 cells in each segment and each data point internal to the box-plot represents one embryo with (□)denoting t=11.5 hours and (○) t=10.5 hours . The total number of embryos is N=6 wild-type and N=5 *hindsight* embryos. (Left to Right) Internal polarization, β-angle and composite aspect ratio comparison for snapshot of time.

drastically and although there is a significantly different A3 internal polarization ($p<0.05$), the overall magnitudes are comparable and within a reasonable range expected from the end of germ band retraction extrapolated from Figure 2-6. Likewise, germ band cell shape is not significantly different in *hnt* from the wild-type embryo when looking at aspect ratio (Figure 2-8). Perhaps most interesting is the results for the angle of minimum tension. Even in the absence of amnioserosa and loss of segment organization within the germ band, the overall direction of internal polarization in the germ band remains consistent with wild-type embryos and with results from Figure 2-8.

Discussion

During germ band retraction there is a clear trend across all analyzed segments (A2, A4, A6, and A7) of increased polarization at mid-retraction. The direction of polarization also confirms the hypothesis that internal polarization acts to oppose the direction of external stress during stable retraction[11,12].

In *hnt* mutants, germ band cells were still measured to be elongated relative to the start of retraction. In the absence of external stress, this elongation was hypothesized to be due to the change in direction of internal polarization. However, the direction of internal polarization remains unchanged in *hnt* mutants.

The degree of polarization in the fixed wild-type embryos after retraction showed that the increased internal polarization does not revert back to the levels seen at the start of retraction. Additionally, it has been shown that in embryos that started dorsal closure

(t~11 hours) there is a large variability in internal polarization between embryos. Although previous studies have found up to a 30% variation between different embryos,[53] it does not fully explain variability in the *hnt* analysis such as that seen in the aspect ratio. The variability between samples during dorsal closure could be due to variation in the internal system that controls cytoskeleton connection in the germ band. Kiehart *et al.* has shown through laser ablation studies that the germ band is under anisotropic tension during dorsal closure.[58] This tension is directed strongest along the axis of elongation (dorsal-ventral direction).[58] This means that internal polarization measured by β-θ analysis is in the direction of elongation similar to germ band extension and potentially acts to retard progress of the leading edge.

A novel use of β-θ analysis was applied to a system that was altered genetically to manipulate germ band mechanics during retraction. The *hnt* mutants were investigated at cellular resolution for the first time in order to image changes in germ band cell shape during retraction in the absence of the amnioserosa. *Hnt* embryos were characterized as having fully or partially deteriorated amnioserosa during mid to late germ band retraction, as well as looser germ band segmentation and a complete failure to retract. In many embryos, germ band segments moved to populate the space previously occupied by the deteriorated amnioserosa. Further, this movement took place in the presence of nominal levels of internal polarization oriented in the same direction as wild-type embryos in both retraction and dorsal closure. This result contradicts a hypothesis by Lacy *et al.* that in the absence of the amnioserosa, the germ band would exist in a state of prolonged, stationary

contraction.[11] In the absence of external stress from the amnioserosa, the germ band in the

hnt mutant embryos maintained an aspect ratio and internal polarization not significantly

different from wild-type. Furthermore, if germ band tension without external stress from

the amnioserosa is proven to yield both protracted contraction as well as movement to fill

in the dorsal region previously occupied by the amnioserosa, it alludes to a novel

mechanism resulting in tissue movement while maintaining internal polarization.

The direction and magnitude of internal polarization in *hnt* embryos provides evidence to

the hypothesis that the signaling for the germ band to undergo internal polarization is

generated from within the tissue and does not involve signals from the amnioserosa. The

results for angle of minimum tension in *hnt* embryos indicate that despite the absence of

amnioserosa, the internal mechanism responsible for internal polarization in the germ

band was unaffected. This has been confirmed in previous experiment by Lynch *et al.* in

isolated patches of germ band cells. It is also qualitatively supported by the images in

Figure 2-7 that lack amnioserosa, but germ band cells have continued to elongate in the

proper direction.   The germ band cells are even seen over time closing up the space the

amnioserosa previously occupied.   This result points to the need for further investigation

into the internal mechanism behind germ band elongation.

Previous studies have shown that the amnioserosa puts physical stress on the entire germ

band[3,12]. This result combined with my analysis showing the germ band provides its own

internal force points to a cooperative model that requires a physical link between external

and internal forces for normal retraction. The necessity of the internal germ band force is seen in the *hnt* experiments where germ band cells still generate their own internal anisotropy and in the direction of elongation completely in the absence of amnioserosa. There are several interesting possibilities for this internal polarization and movement. One possibility could be a third force on the germ band perhaps from beneath the tissue from the basement membrane, which is not directly taken into account in the β-θ model other than as a constraint on the cell volume. Wound healing models have demonstrated epithelial cells ability to crawl with lamellipodia to close a wound. The use of lamellipodia has been demonstrated during germ band retraction in the amnioserosa, which maintains a connection by crawling over segment A9[3]. Lamellipodia have been found to be crucial in driving cell intercalation to generate internal tension in the germ band during extension[59]. In the absence of a change in polarization direction, germ band movement may still be directed by lamellipodia crawling over the basement membrane in a wound healing type response.

Chapter 3

Pharmacokinetics and Bioavailability in PDMS-based Microfluidic Devices

Authors of Manuscript

Alexander W. Auner, Kazi Tanseem, Dmitry A. Markov, Lisa J. McCawley, and M. Shane

Hutson

Abstract

Microfluidic organ-on-chip devices constructed from polydimethysiloxane (PDMS) have

proven useful in studying both beneficial and adverse effects of drugs, supplements, and

potential toxicants. Despite multiple advantages, one clear drawback of PDMS-based

devices is adsorption of chemicals through exposed surfaces. Chemical binding to PDMS

creates problematic changes in dose response curves and timing of chemical delivery to

cells. Molecular agents used in lab-on-chip devices have been tested in recent efforts to

quantify PDMS binding. Eight chemicals were identified to bind to PDMS out of the

nineteen used in our applications with both visible light and infrared absorption

spectroscopy. Quantitative relationships for chemical partitioning into PDMS were

established through fitting spectroscopic data to a microscopic model of binding kinetics and extracting time dependent adsorption coefficients, saturation amount and forward and reverse rate constants. The relationship between chemical partitioning and select molecular properties was investigated, and we have shown a combination of the octanol-water partition coefficient (Log P) and H-bond donor number to be a decent predictor of absorption for chemicals with Log P >1.8. Experimental rate constants were used to model adsorption due to continuous and bolus exposure of several chemicals in a realistic device geometry. From this analysis, we determined that in order for cells to not be over- or under-dosed by up to an order of magnitude, timing of delivery is critical.

Introduction

Microfluidic organ-on-chip devices have proven useful in studying both beneficial and adverse effects of drugs, supplements, and potential toxicants through improved response times and reduced costs in bioactivity screens.[34] Such devices have also been used to investigate chemical effects in models for a range of biological systems and processes: e.g., mammary glands;[60] lungs;[37] hepatotoxicity;[38] renal differentiation;[39] and multi-organ coupling.[36] The primary polymer used to fabricate microfluidic devices has been polydimethysiloxane (PDMS). The advantages of PDMS range from its optical transparency to its gas permeability to its ease of fabrication and relatively soft mechanical properties.[61] Compared to rigid glass or plastic substrates, cells cultured in PDMS-based devices encounter a somewhat porous, elastic environment much more similar to that experienced *in vivo*.[24,25]

Despite these advantages, one clear drawback of PDMS is its hydrophobicity. This disadvantage is particularly worrisome in chemical screening applications because hydrophobic compounds can bind to or become sequestered within PDMS. Such binding causes a discrepancy between the nominal inlet concentration and actual cellular exposures, affecting dose-response curves and estimates of the Lowest Observed Adverse Effect Level (LOAEL). The aims of this study are to characterize those chemical properties that are predictive of PDMS binding, to present a simple protocol for experimentally measuring the on- and off-rate PDMS-binding kinetics, and to show how the measured kinetic parameters can be used to model chemical transport in PDMS-based devices to predict and/or design actual cellular exposures.

The binding and sequestration of hydrophobic compounds by PDMS was first investigated qualitatively using fluorescent molecules.[62] Subsequent quantitative studies suggested relationships between a compound's degree of PDMS binding and its octanol/water partition coefficient (LogP) or its topological polar surface area (TPSA). One study suggested a LogP threshold – strong binding for highly hydrophobic compounds with LogP > 2.62.[63] The follow-up, which only tested compounds above the LogP threshold, suggested a linear correlation of stronger binding with smaller TPSA.[64] These two studies were limited to evaluation of just 5 and 4 compounds, respectively. To further investigate the link between molecular properties and chemical partitioning into PDMS, we have chosen a larger, more diverse sample of 19 test compounds. These chemicals have a range of uses – from pesticides to pharmaceuticals to the manufacture of consumer products – and were

Table 3-1: Commerical use and toxicity references for chemicals tested here.

Chemical Name	Use	Toxicity in Mammals	Ref.
perfluorooctanoic acid (PFOA)	Teflon™ manufacturing	Endocrine disruptor	[65–72]
bisphenol A	Plastic manufacturing	endocrine disruptor	[65,73–81]
diethylstilbestrol	synthetic non-steroidal estrogen	endocrine disruptor	[82]
genistein	pharmaceutical/ supplement	endocrine disruptor	[83–86]
secoisolariciresinol diglucoside (SDG)	pharmaceutical/ supplement	non-toxic	[87]
doxorubicin	chemotherapy	cytotoxic	[88]
docetaxel	chemotherapy	cytotoxic	[88]
propiconazole	fungicide	reproductive	[65]
aminopyralid	herbicide	developmental	[89]
molinate	herbicide	reproductive	[65,90]
ethofumesate	herbicide	non-toxic	[91]
imazaquin	herbicide	non-toxic	[89]
hexazinone	herbicide	reproductive	[89]
foramsulfuron	herbicide	non-toxic	[89]
sulfentrazone	herbicide	reproductive	[65]
acetamiprid	insecticide	reproductive	[65]
formetanate	insecticide	neurotoxin	[89]

selected due to their use in current organ-on-chip toxicology studies. As detailed in

Table 3-1, many of the test compounds have been linked to endocrine disruption and

developmental or reproductive toxicity; others serve as negative controls with no

known toxicity in mammals. To interpret the results of toxicology studies using

these compounds in PDMS-based microfluidic devices, it is crucial that we can

accurately predict their in-device bioavailability.

Such predictions will rely on computational models. Here we provide a simple

method for measuring the needed model parameters for reversible and irreversible

PDMS-binding kinetics. These include the forward and backward rate constants, as

well as chemical-specific carrying capacities per unit of PDMS surface area. Previous

approaches to this problem explicitly modelled diffusional transport of chemicals

within PDMS;[92] however, we find that the combined effects of partitioning at the

solution-PDMS interface and diffusion into the PDMS bulk are well described by rate

constants and carry capacities over tens to hundreds of hours. For most tested

compounds, we used time-resolved UV-Vis absorption spectroscopy to monitor

depletion (and later return) of chemical from (to) a solution in contact with either a

PDMS disk or the walls of a PDMS microfluidic channel. For one chemical,

perfluoorooctanoic acid (PFOA), we instead used FTIR spectroscopy in attenuated

total reflectance (ATR) mode to directly measure accumulation on a PDMS surface.

Once the parameters are measured, we then present a model that combines

computational fluid dynamics (CFD) with PDMS-binding kinetics to predict chemical

bioavailability in a simple microfluidic device. These predictions include

temporally- and spatially-varying chemical concentrations in the perfusion media, as well as the effective suface density of bound chemical throughout the device. We use this model to highlight what typical PDMS-binding parameters imply for bioavailability. Our approach complements prior work that focused on microfluidic design considerations for minimizing the impact of sequestration in PDMS.[92] These design considerations depended on the properties of the chemicals to be tested – *e.g.*, partition and diffusion coefficients – and are thus not as useful when designing a single microfluidic system to test a wide range of drugs or potential toxicants. Explicitly modeling bioavailability for each chemical is thus a key step towards pharmacokinetics for organ-on-chip or microphysiological systems.

Experimental Design

PDMS Preparation
PDMS Sylgard 184 (Dow Corning, Auburn, MI) was mixed with a 1:10 weight ratio of curing agent to elastomer. Air bubbles were removed and the mixture was cured for 24 hours. Bulk PDMS was cast in a 5-mm thick layer and cut into cylindrical sections (6-mm in diameter) in preparation for chemical soaking for disk experiments. For channel experiments, PDMS was cast in a 3-mm thick layer over the channel mold, which was fabricated using standard photolithography on Si wafer with SU8-2050 photoresist. Channels were completed by punching 1.5 mm diameter cylindrical reservoirs at both ends of the channel and placing a 3-mm thick layer of PDMS on the top and bottom of the channel to seal the input and output reservoir by self-adherence. Channel dimensions are given in Figure 3-1B.

Chemical Preparation

All chemicals were purchased in powder form (except liquid molinate) from Sigma Aldrich

(Saint Louis, MO). Chemicals to be tested were dissolved in either molecular biology grade

water or a 1X phosphate buffered saline (PBS) solution with added 0.1% dimethyl sulfoxide

(DMSO) to increase solubility of hydrophobic compounds (LogP >1). Chemicals were

diluted in their respective solvent to starting concentrations that yielded a peak UV-Vis

absorbance of one or as close as solubility allowed. Molecular properties were provided by

the EPA Chemistry Database,[89] Canadian Institute of Health Toxin Database,[93] University of

Hertfordshire Pesticide Properties Database,[94] and select publications for genistein.[95]

Experimentally measured LogP was used in all cases except PFOA, formetanate, and SDG,

for which cLogP was used in the absence of published experimental data.

UV-Vis Measurements

For disk-soak experiments, UV-Vis absorbance measurements were taken using a Cary

5000 dual-beam UV-Vis spectrometer (Agilent, Santa Clara, CA) with a scan rate of 24

nm/min and a resolution of 1 nm. For on-rate measurements, sample solutions were

placed in 4-ml quartz cuvettes with cylindrical disks of PDMS floating just below the

solution surface. When spectra were not being measured, the cuvettes with floating PDMS

disks were placed on an orbital shaker. When spectra were being measured, the disks

remained in the cuvettes, but above the spectrometer light beam (Figure 3-1). The

reference beam contained a matched cuvette with appropriate solvent. For off-rate

measurements, PDMS disks were removed from sample-solution cuvettes and dried with

nitrogen. Each pre-soaked PDMS disk was then transferred to float atop appropriate fresh

solvent in a new cuvette for collection of additional spectra. To control for chemical

stability, time-resolved spectra were also taken of positive control cuvettes containing

sample solutions without PDMS. To correct for instrumental baseline drift, time-resolved

spectra were concomitantly measured for negative control cuvettes containing PBS + 0.1%

DMSO.

For channel-soak experiments, chemical solutions were pipetted out of the channel and

measured using a Nanodrop 2000C Spectrophotometer (Thermo Fisher, Waltham, MA).

Time-resolved measurements were obtained by sealing individual channels for different

periods of time. Each time-point measurement was repeated in triplicate.

For both spectrometers, in order to convert from absorbance to chemical concentration, a

clearly discernible peak of interest was selected from spectra at several chemical dilutions

and then used to construct a linear calibration curve (measured in triplicate for each

chemical).

FTIR Measurement

The UV-Vis absorption band for one tested chemical, PFOA, was too near the edge of UV

detection for reliable measurement. As an alternative, we took IR spectra to measure PFOA

bound to PDMS disks using a Nicolet IS5 FTIR spectrometer (Thermo Fisher, Waltham, MA)

with a single-reflection diamond ATR attachment. Measurements were averaged 100 times

with a resolution of 4 cm^{-1} and with the evanescent wave covering a 1.5-mm diameter area.

PDMS disks were soaked in a solution of PFOA for 48 hours, removed from solution, dried

with nitrogen, and placed directly onto the diamond ATR. Both PFOA-soaked disks and

control solvent-soaked disks were measured in triplicate to confirm homogeneity of

surface binding. Since FTIR spectra were measured at a single time point, they were only

used to estimate the amount of PFOA bound and not its binding kinetics. To convert from

IR absorbance to concentration, we used the strong PFOA vibrational mode at 1209 cm^{-1},

which corresponds to a $(CF_2)+(CF_3)$ asymmetric stretch,[96] and measured calibration

spectra of diluted PFOA solutions in pure DMSO. The contribution of PDMS to FTIR spectra

of soaked disks was minimized by weighted subtraction of a spectrum of a control solvent-

soaked disk and a constant baseline offset, with weights determined by least squares

minimization of the resultant spectrum in a region with no PFOA vibrational bands (990-

1040 cm^{-1}).

Computational Model

Modelling of chemical transport in a microfluidic device, including binding and desorption

from PDMS surfaces, was conducted using COMSOL Multiphysics (Burlington, MA). The

modelled geometry was a single longitudinal plane through a simple rectangular

microchannel (length = 8 mm, width = 1.5 mm, and height = 0.1 mm). Since channel width

was much greater than height, variations in velocity and concentration along the channel

width were neglected and a well-developed 2D parabolic flow velocity was imposed

vertically. This 2D approximation is reasonable for our geometry; fluid velocities in 2D and

full 3D models differ by less than 5% over the middle 87% of the channel width. Symmetry

allowed for a further reduction in computation time by explicitly modelling only the

bottom half of the channel. Conditions were assumed to be isothermal, with convective flux

boundary conditions specified at both device inlet and outlet. The model scheme was

validated by simulating disk-soak experiments under well-mixed conditions to reproduce the experimental binding and desorption kinetics.

Results

The primary method used here to measure chemical binding to PDMS was quantifying the loss of chemical from a solution in contact with a PDMS disk or channel surface using UV-Vis absorbance (Figure 3-1). Control experiments on matched solutions without PDMS disks confirmed that all but one tested chemical had no significant PDMS-independent degradation or precipitation. That exception was molinate. Its precipitation in control experiments was measured and its binding to PDMS was assessed as the excess depletion observed in disk-soak experiments.
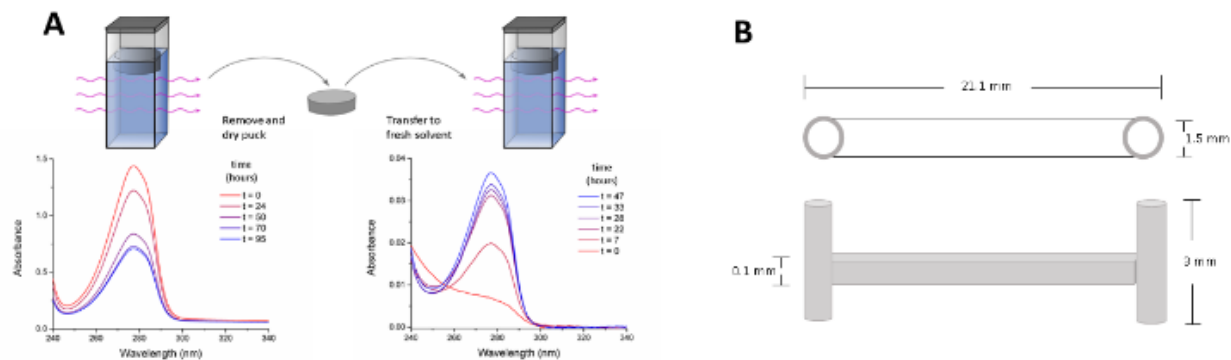
Figure 3-1: PDMS-binding and desorption experiments with example spectra for ethofumesate. (A-left) UV-Vis spectra showing depletion of ethofumesate from bulk solution as it partitions into a PDMS disk floating in the cuvette. (A-right) UV-Vis spectra showing return of ethofumesate to bulk solution as it desorbs into fresh solvent from a pre-soaked PDMS disk. (B) Dimensions of the microfluidic channel used in channel-soak experiments.

We observed no PDMS binding for any tested chemical with LogP < 2.5. On the other hand, several of the more hydrophobic chemicals were lost from solution with a roughly

exponential decay over tens of hours – as shown in Figure 3-2 for molinate, ethofumesate, propiconazole, and to a lesser degree, bisphenol A. This behavior was not universal: other hydrophobic chemicals with LogP > 2.5, such as diethylstilbestrol and genistein, showed no evidence of depletion from solution and thus no binding to PDMS. The most hydrophobic compound tested, PFOA, had no appropriate UV-Vis absorption, which precluded
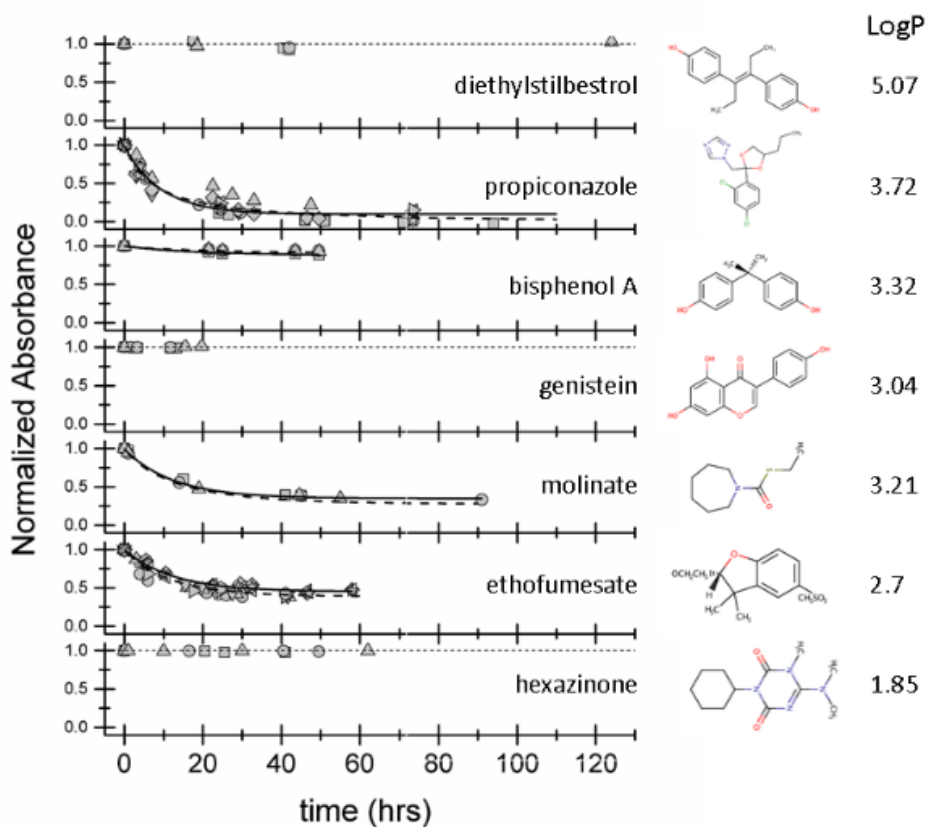
Figure 3-2: Time-dependent depletion of select chemicals from bulk aqueous solutions in PDMS disk-binding experiments. Results ordered via descending LogP (listed beside each chemical structure). Data points with different symbols indicate different replicates. Solid lines are best fits to an empirical description (Equation 3-1); dashed lines are fits to a microscopic model for binding kinetics (Equation 3-3). Dotted lines show a normalized absorbance of 1.0 for chemicals with no discernible depletion.

measuring its binding kinetics, but we were able to measure the degree to which it bound

PDMS at a single time point using ATR-FTIR spectroscopy. We found that 24% of the PFOA

originally in solution had bound to the surface of a PDMS disk after soaking for 48 hours.

When pre-soaked PDMS disks were transferred to fresh solvent, we found that two tested

chemicals desorbed from PDMS and returned to solution: molinate and ethofumesate. As

shown in Figure 3-3, their desorption followed a roughly exponential approach to a new

equilibrium between bound and free chemical. Respectively, about 1/4 and 1/3 of the
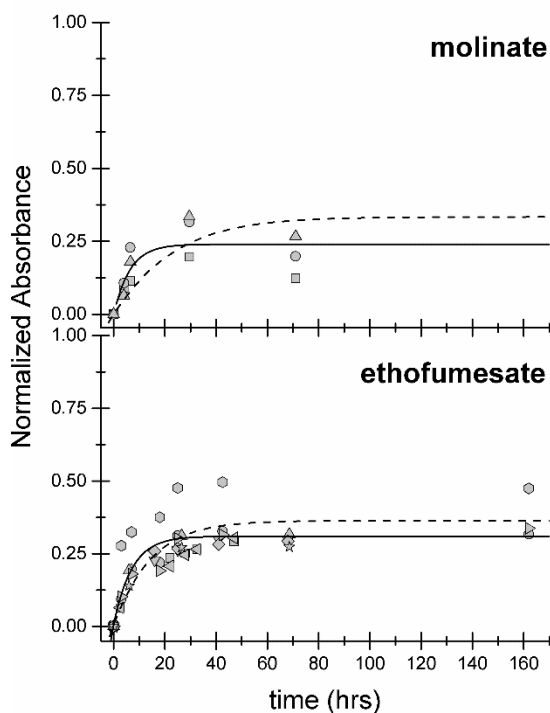
Figure 3-3: Time-dependent return of chemicals into bulk aqueous solution via desorption from previously-soaked PDMS disks. Different symbols denote different experimental replicates. Solid lines are best fits to an empirical description (Equation 3-2); dashed lines are fits to a microscopic model of binding kinetics (Equation 3-3). Absorbance is normalized to the amount depleted from solution, and thus bound to the disk, in the previous soaking experiment (44.4 μM for ethofumesate; 53 μM for molinate).

molinate and ethofumesate bound to a PDMS disk returned to solution within 48 hours. The other two chemicals for which we could measure PDMS-binding kinetics, namely propiconazole and bisphenol A, bound irreversibly with no evidence of desorption in fresh solvent.

To empirically quantify the PDMS-binding kinetics of each chemical, we fit the disk soak results to exponential approaches to equilibrium:

$$A = A_0 + \Delta A_1\left(1 - e^{-t/\tau_1}\right) \tag{3-1};$$

$$A = \Delta A_2(1 - e^{-t/\tau_2}) \tag{3-2}.$$

Equation 3-1 fits experiments in which an initial amount of chemical A_0 is depleted from solution with time constant τ_1 to approach a final value of $A_0 + \Delta A_1$ (in which $\Delta A_1 < 0$). Equation 3-2 similarly fits experiments in which an amount of chemical $\Delta A_2 > 0$ returns to solution as it desorbs from a pre-soaked disk with time constant τ_2. For each chemical that bound PDMS, Table 2 lists the time constants (τ_1, τ_2), the fraction bound at equilibrium, $f_{B,eq}$ = $-\Delta A_1/A_0$, and the fraction eventually returned to solution, $\Delta A_2/A_0$. For chemicals that did not exhibit significant loss from solution, the fraction bound represents a lower limit in detectable percentage change in absorbance between the start and endpoints of the experiment. Note that these are empirical descriptors specific to the stated experimental conditions.

Notably, Rhodamine B did not show significant binding to PDMS in disk-soak experiments despite visibly dying the disk surface. To measure binding for chemicals that bound PDMS

more weakly, we thus conducted additional experiments in which solutions were sealed inside a microfluidic channel (dimensions as in Figure 3-1). These channel-soak experiments had a much larger surface-to-volume ratio (116 cm^{-1} versus 0.3 cm^{-1}), which allowed detection of weaker binding. Results from both types of experiments are compared in Table 2. Due to the s+horter effective pathlength of the Nanodrop spectrophotometer, several chemicals had too little absorbance even at their solubility limit to have their PDMS binding measured using channel-soak experiments (diethylstilbestrol, propiconazole, molinate, ethofumesate, docetaxel).

Our model of chemical binding to PDMS assumes the solution is well-mixed at all time in the vicinity of the PDMS surface. This requires a fast chemical diffusion time relative to the binding characteristic time. In order to test this assumption, rhodamine B was pipetted into a cuvette filled with PBS solution and mixing at the center of the cuvette was measured over time (Figure 3-4). The characteristic time of diffusion was measured to be ~2 hours, roughly an order of magnitude smaller than most chemicals binding times (Table 2). Diffusion time significantly increased when the cuvette was placed on a rocker in between
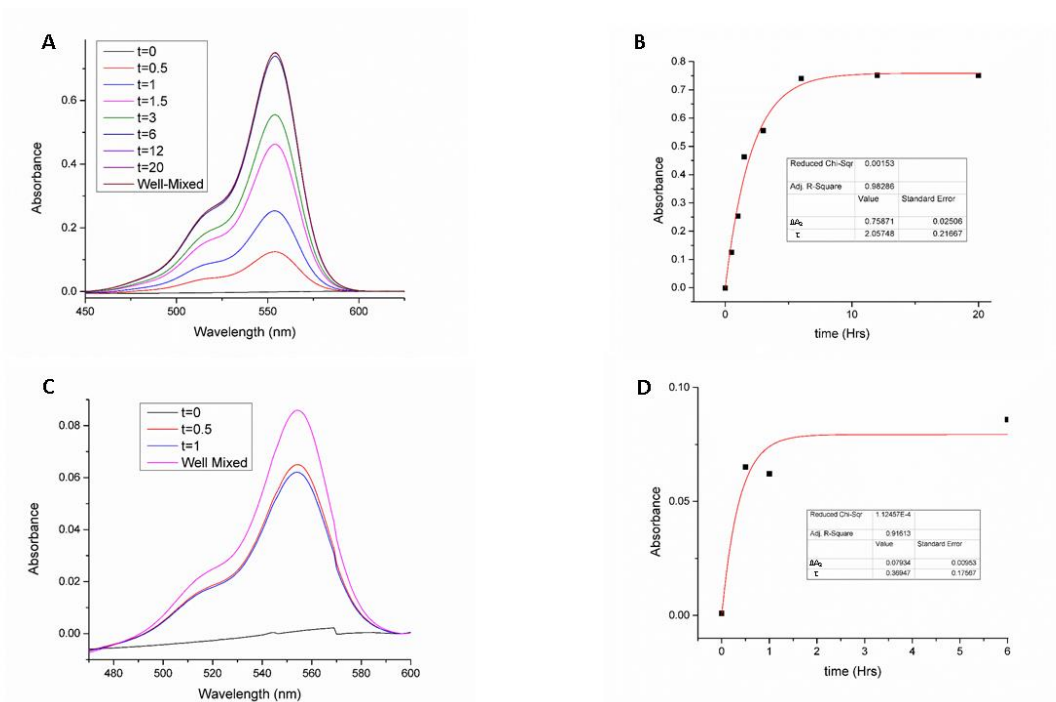
Figure 3-4: Diffusion of rhodamine B into PBS filled cuvette over time. (A, C) rhodamine B absorbance spectra over time as the chemical mixes into the solution. (B, D) Fit from equation 3-2 to peak absorbance over time for stationary cuvette (B) and gently rocked cuvette (D).

measurements. The resulting characteristic time was ~0.3 hours, another order of magnitude smaller. With these results in consideration, the assumption that diffusion takes place quick enough to replenish lost chemical at the PDMS surface is reasonably valid for our experimental set-up.

The eight chemicals in our test set that measurably bound to PDMS in either experiment all had high LogP (≥ 2.7) and low TPSA (≤ 70.2 Å^2). These results are consistent with data from two previous studies by Wang *et al.* and Van Meer *et al.* that linked PDMS absorption

to measures of high hydrophobicity.[63,64] On the other hand, our larger test set identified

several chemicals with similarly high LogP and/or low TPSA that did not measurably bind

to PDMS, e.g., diethylstilbestrol and genistein (LogP of 5.07 and 3.04 respectively; see Table

2). We thus investigated whether any additional molecular property would distinguish the

hydrophobic non-binders. The only combination we found that discriminated binders from

non-binders was LogP and the number of H-bond donors. This discrimination is shown in

Figure 3-5, which separately compares results for disk-soak experiments and channel-
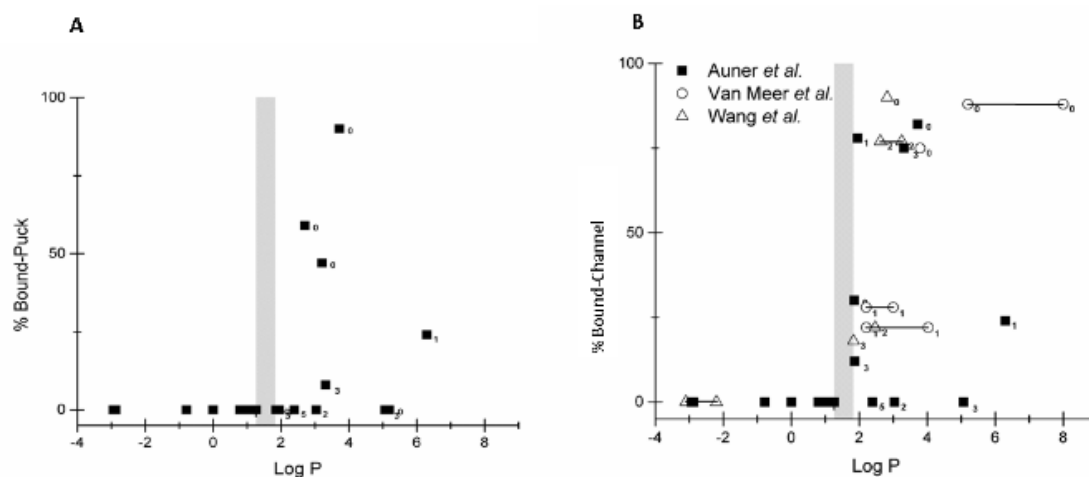
Figure 3-5: Correlation of PDMS binding affinity (% Bound) with chemicals' LogP and number of H-bond donors (subscript). Shaded region represents the LogP threshold for significant chemical absorption. (A) Disk-soak experiments. (B) Channel-soak experiments reported in this work (■), in van Meer *et al.*[47] (○), or in Wang *et al.*[46] (△). Data points connected with horizontal lines denote discrepancies in reported LogP values.

Table 3-2: Summary of experimental results for all chemicals tested

Molecular Properties			Disk Exp. Detail		Disk Empirical Fit Parameters				Channel Exp. Detail		Channel Empirical Fit Parameters			
Chemical Name	Log P	TPSA (Å²)	N	A_0 (µM)	$f_{B,eq} = -\Delta A_1/A_0$	τ_1 (h)	$\Delta A_2/A_0$	τ_2 (h)	N	A_0 (µM)	$f_{B,eq} = -\Delta A_1/A_0$	τ_1 (h)	$\Delta A_2/A_0$	τ_2 (h)
PFOA	6.3	37.3	5	589	26±4%	--	--	--	-	--	--	--	--	--
rhodamine 6G	5.2	59.9	2	20	1.9±0.3%	--	--	--	5	189	8±3%	--	--	--
diethylstilbestrol	5.07	40.5	3	89	4±3%	--	--	--	-	--	--	--	--	--
propiconazole	3.72	49.2	9	336	90±2%	9.7±1	--	--	-	--	--	--	--	--
bisphenol A	3.32	40.5	3	97	8±2%	17.6±1	--	--	3	488, 3100	78±1%	3.12±0.03	11.8±2%	0.2±0.2
genistein	3.04	87.0	3	38	0.70±0.04%	--	--	--	3	38	4±4%	--	--	--
molinate	3.21	45.6	3	113	50±10%	13.6±2	12±2%	6.1±1	-	--	--	--	--	--
ethofumesate	2.7	70.2	9	75	59±4%	11.3±1	19±1%	11.0±2	-	--	--	--	--	--
docetaxel	2.40	224.0	1	930	-0.2±0.2%	--	--	--	-	--	--	--	--	--
rhodamine B	1.95	52.8	3	10	2.05±0.05	--	--	--	3	177	80±5%	2.6±0.7	5±2%	1.5±0.8
imazaquin	1.86	91.6	1	17	-2.8±0.5%	--	--	--	3	16	13%	3.5±0.8	--	--
hexazinone	1.85	56.2	3	40	1.1±0.6%	--	--	--	3	40	37±7%	2.8±0.6	--	--
doxorubicin	1.27	206	1	60	7±2%	--	--	--	2	60	5±8%	--	--	--
sulfentrazone	0.99	90.5	1	26	-3±1%	--	--	--	2	26	-8.00±0.02%	--	--	--
acetamiprid	0.8	52.3	1	45	0.5±0.1%	--	--	--	2	45	-1±8%	--	--	--
formetanate	0	53.9	1	39	-0.6±0.3	--	--	--	2	39	-9±3%	--	--	--
foramsulfuron	-0.78	177.0	1	32	0.8±0.4%	--	--	--	2	32	7±3%	--	--	--
aminopyralid	-2.87	76.2	1	50	-8±2%	--	--	--	3	50	-14±7%	--	--	--
SDG	-2.93	258	1	58	-0.29±0.05	--	--	--	2	58	11±9%	--	--	--

soak experiments reported here and in previous studies. Whenever there was a

discrepancy in reported LogP values, we plotted data points at both values and connected

them with a horizontal line. There is clearly a threshold LogP (in the range of 1.27-1.83),

below which chemicals do not bind PDMS. Above this threshold, chemicals may bind

PDMS, but the strength of this binding decreases for molecules having more H-bond

donors. An exception to this trend was rhodamine 6G as tested by Wang *et al.*[11] We tested

rhodamine 6G in both our experimental setups and found no measurable binding to PDMS.

This discrepancy will be revisited in Discussion.

Predicted Impact of Chemical-PDMS Binding

As noted above, the empirical descriptors of PDMS binding are useful, but specific to

limited experimental conditions. To find parameters more useful for modelling chemical-

PDMS interactions over a wider range of concentrations and PDMS surface areas, we fit the

data to a microscopic model of binding kinetics. The model binding may be reversible with

forward and backward rate constants (k_F, k_R). The governing differential equation is thus:

$$\frac{dA(t)}{dt} = -k_F A(t) \left(\frac{S_0}{\alpha} - \left(A_{tot} - A(t) \right) \right) + k_R (A_{tot} - A(t)) \qquad (3\text{-}3)$$

where $A(t)$ is the chemical concentration in solution and α is the ratio of solution volume to

PDMS surface area. For a given chemical, binding and desorption experiments were fit

simultaneously with shared parameters. Binding experiments were fit to analytic solutions

Table 3-3: Summary of microscopic model fit parameters

Chemical	k_F (10^{-4} h^{-1} μM^{-1})	k_R (10^{-2} h^{-1})	S_0 (nm^{-2})
propiconazole	3.7 ± 0.7	0	7300 ± 600
bisphenol A	0.3 ± 0.2	4.6 ± 0.7	500 ± 300
molinate	5 ± 1	0.9 ± 0.2	2500 ± 300
ethofumesate	5 ± 2	2.27 ± 0.4	2000 ± 1000
rhodamine B	3.2 ± 0.3	0.003 ± 0.002	8.0 ± 0.3
imazaquin	1.5 ± 0.5	0	0.13 ± 0.03
hexazinone	7 ± 2	0	0.7 ± 0.1

to Equation 3-3 using boundary condition $A(0) = A_{tot}$ = the stated starting concentration. Desorption experiments were fit to solutions with $A(0) = 0$ and A_{tot} being the amount bound to the disk surface at equilibrium in the matched binding experiment. For chemicals that bound irreversibly, the desorption experiment was simply taken to yield $k_R = 0$. Microscopic model fits are shown alongside the empirical fits of binding/desorption kinetics in Figures 3-2 and 3-3. Parameters from the microscopic model fits are compiled in Table 3.

These microscopic model fit parameters were then used in a computational fluid dynamics (CFD) model combining mass transport and surface reactions to predict the sequestration of chemicals in a PDMS-based microfluidic device (geometric details under Experimental Design). This model is very similar to those used in biosensor applications.[97–101] Chemical transport in the bulk fluid is described by a convection-diffusion equation:

$$\frac{\partial c}{\partial t} = D \left(\frac{\partial^2 c}{\partial x^2} + \frac{\partial^2 c}{\partial y^2}\right) - c \cdot \vec{u} \tag{3-4}$$

where c is the time-dependent chemical concentration, D is the diffusivity of the chemical

species in the bulk, and u is the position- and time-dependent fluid velocity. Chemical

transport and reaction on the PDMS surface are governed by a reaction-diffusion equation:

$$\frac{\partial c_s}{\partial t} = D_s \left(\frac{\partial^2 c_s}{\partial x^2} + \frac{\partial^2 c_s}{\partial y^2}\right) + k_F c(\theta_s - c_s) - k_R c_s \tag{3-5}$$

where c_s is the bound species surface density, D_s is its surface diffusivity, θ_s is the carrying

capacity per unit of PDMS surface area, and k_F, k_R are the forward and backward rate

constants for surface binding respectively. This model does not explicitly consider

diffusion into bulk PDMS, but chemicals with higher PDMS diffusivity would correspond to

larger carrying capacities. The surface reaction expression in Eqn. 5 includes the bulk

concentration, c, at the reacting surface. This coupling with mass balance in the bulk is

obtained at the flux boundary according to

$$D \left(\frac{\partial c}{\partial y}\right) = k_F c(\theta_s - c_s) - k_R c_s \tag{3-6}$$

To explore the potential range of binding and chemical sequestration, we ran this model for

three tested chemicals: rhodamine, which is minimally adsorbed by PDMS; ethofumesate,

which binds reversibly; and propiconazole, which binds irreversibly. Since these chemicals

were of similar size, their diffusivities were taken to be the same: 10^{-9} m^2/s in aqueous

solution (D) and 10^{-11} m^2/s along the PDMS surface (D_s). Each model considered parabolic

flow with a maximum velocity, u_{max} = 100 μm/s. Cellular exposure is taken as the chemical

concentration just above the PDMS surface at the end of the 8-mm long channel (where a

cell culture chamber would begin). We investigated effects under both continuous

injection of chemicals (starting from t = 2 hours) and bolus injections (from t = 2 to 6

hours) over a wide range of inlet concentrations from 10^{-2} to 10^{-7} M. Inlet concentrations

for ethofumesate and propiconazole were limited to < 10^{-4} M due to their low aqueous

solubility. Predicted cellular exposures are shown for all three chemicals for continuous

and bolus injections in Figure 3-6A-C and 3-6A-C, respectively. These figures also include

the corresponding degree to which PDMS binding sites are saturated (Figure 3-6D-F, 3-7D-

F).
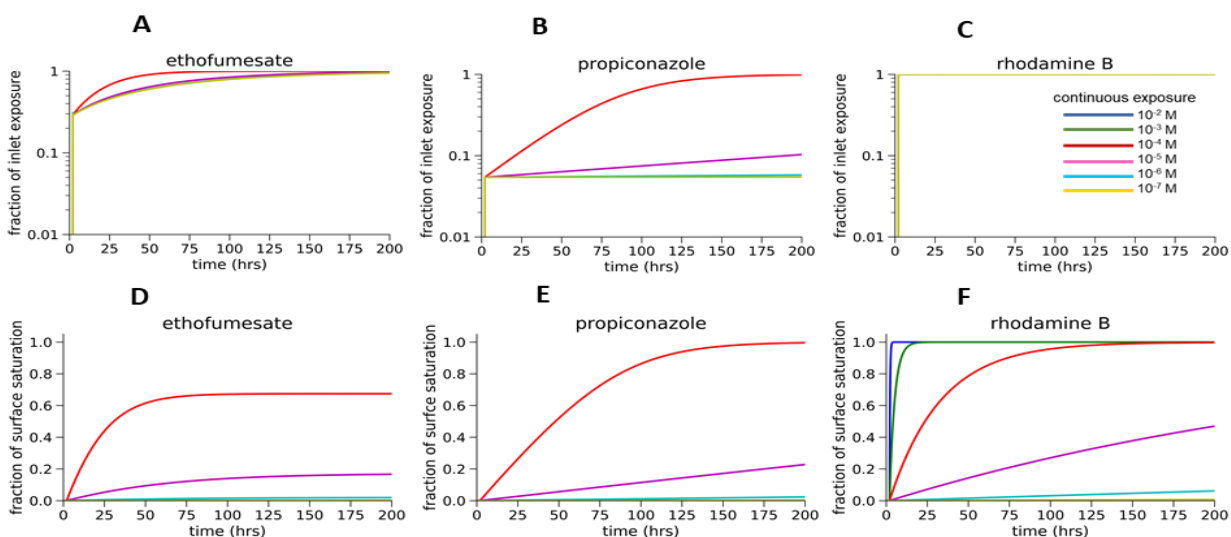
Figure 3-6: CFD model predictions for continuous dosing with inlet concentrations from 10^{-7} to 10^{-2} M: (A-C) predicted cellular exposures as a fraction of inlet exposures; (D-F) predicted degree of PDMS surface saturation. Chemical classes represented by ethofumesate with strong reversible binding, propiconazole with strong irreversible binding, and rhodamine B with weak reversible binding. Legend in (C) applies for all panels.
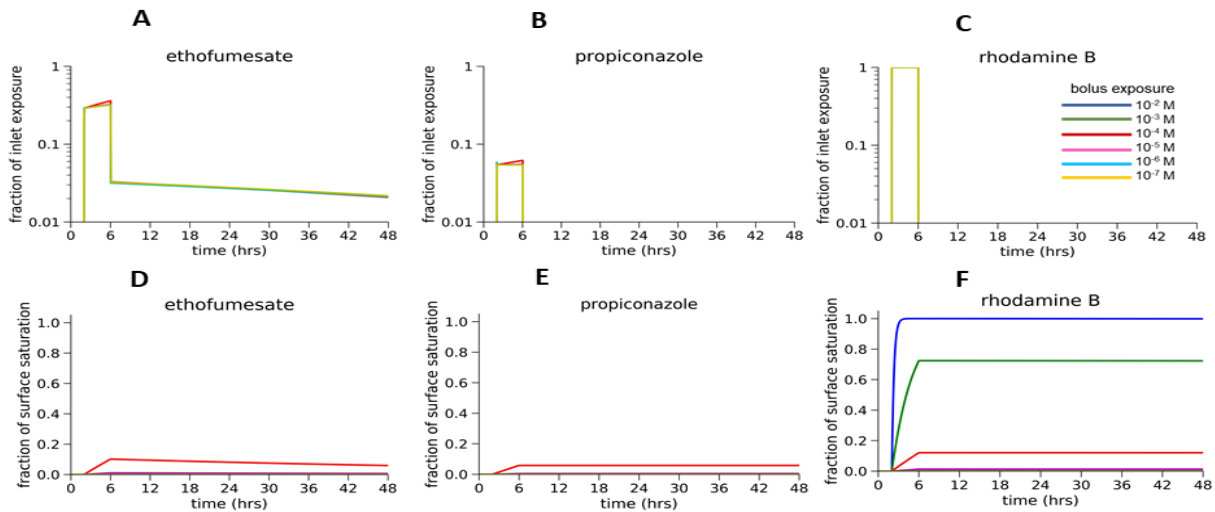
Figure 3-7: CFD model predictions for 4-h bolus dosing with inlet concentrations from 10^{-7} to 10^{-2} M: (A-C) predicted cellular exposures as a fraction of inlet exposures; (D-F) predicted degree of PDMS surface saturation.

Under continuous dosing, the differential impacts of reversible and irreversible PDMS binding can be seen by comparing Figure 3-6A,D and 6B,E. For a reversible binder like ethofumesate, the predicted cellular exposure gradually increases with time and asymptotically approaches the inlet concentration (Figure 3-6A). This occurs for all inlet concentrations once the on- and off-rates for PDMS binding approach equilibrium. For the highest inlet concentration simulated (10^{-4} M), this equilibrium occurs at nearly 70%

ighest inlet concentration simulated (10^{-4} M), this equilibrium occurs at nearly 70% surface saturation (Figure 3-6D). On the other hand, for an irreversible binder like surface saturation (Figure 3-6D). On the other hand, for an irreversible binder like propiconazole, the predicted cellular exposures only approach the nominal inlet concentrations once the surface becomes fully saturated (Figure 3-6B,E). Even at the highest dose simulated (10^{-4}

M), reaching saturation can take several hundred hours. For doses that do not yield surface saturation within the simulated time window (200 h), the predicted cellular exposure remains an order of magnitude less than the nominal inlet concentration.

Additional impacts arise under bolus dosing. For a reversible binder like ethofumesate, exposure was at lower levels (less than 30% of inlet exposure) for all of the 4 hour bolus period (Figure 3-7A,D). Even more interestingly, once a bolus dose ended, cellular exposure continued. This extended exposure was due to gradual chemical desorption from the surface. This extended exposure was due to gradual chemical desorption from the surface. It could initially be as large as 5% of the bolus exposure and gradually diminished to less than 1% after 48 hours. Such extended exposures were absent for an irreversible binder like propiconazole, but it too had effects that were highly dependent on the nominal inlet concentration. Only at the highest simulated dose (10^{-4} M) was propiconazole able to saturate the device's PDMS surfaces during the bolus period and thus yield cellular exposures approaching the nominal inlet concentration. For all other simulated doses, the exposures were an order of magnitude less than the nominal dose.

For weaker binding chemicals like rhodamine B, cellular exposures closely match inlet concentrations. This is true for all simulated doses under both continuous (Figure 3-6C,F) and bolus exposures (Figure 3-7C,F). At low inlet concentrations (10^{-7} to 10^{-5} M), the on-
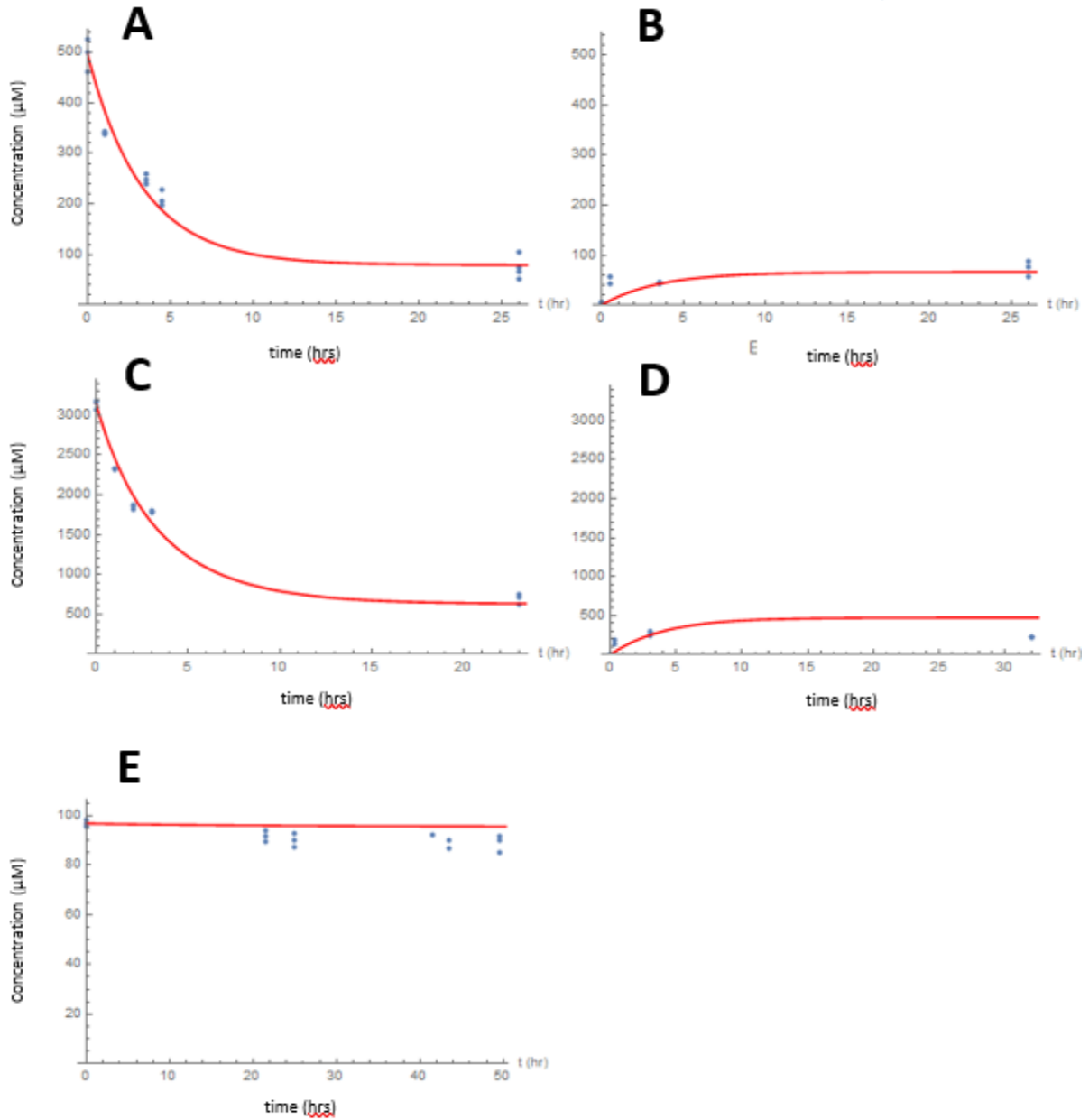
Figure 3-8: Simultaneous fit of microscopic model for binding kinetics (Equation 3-3) to all bisphenol A experiments. (A,B) Adsorption and desorption, respectively, for 488 µM channel experiment, (C,D) adsorption and desorption for 3000 µM channel experiment and (E) adsorption for disk experiment.

rate for binding is so low that there is little impact on cellular exposures under the

modelled flow conditions.   At higher inlet concentrations (10^{-2} to 10^{-4} M), binding is more

rapid and the system quickly reaches surface saturation (Figure 3-6D), but the low binding

capacity of the surface again results in little change in chemical concentrations throughout

the perfusate.

Discussion

Here we have investigated sorption to PDMS surfaces for 19 chemicals of interest in

environmental toxicology. This larger set of test chemicals covers a wider range of

molecular properties than previous studies and allows us to further delineate those

characteristics most closely associated with binding to PDMS. In addition, for those

chemicals that did bind, we have more fully characterized the on- and off-rate kinetics to

facilitate predictive modelling of chemical sequestration and actual cellular exposures in

PDMS-based microfluidic devices.

Importantly, we used two experimental setups, disk soaks and channel soaks, to fully

characterize both weak and strong PDMS affinities. Only one compound in our test set, i.e.,

bisphenol A, was amenable to kinetic characterization in both setups. Given the different

surface-to-volume ratios and starting concentrations, the two experiments for bisphenol A

yielded quite different empirical parameters (% bound and time constants); however, all of

the bisphenol A data could be fit well simultaneously with a single set of microscopic

kinetic parameters (k_F, k_R and S_0) (Figure 3-8). This consistency is an important validation

of the approach taken here.

In terms of the molecular properties that influence PDMS binding, we also find a key role

for measures of chemical hydrophobicity. Wang *et al.* tested five compounds and noted an

apparent LogP threshold separating chemicals that bound PDMS strongly ($\geq$ 2.62) from

those that did so weakly or not at all ($\leq$ 2.47).[63] Van Meer *et al.* tested four other chemicals

– all with LogP above the apparent threshold – and instead noted a linear correlation

between the percent remaining unbound to PDMS and the compounds' TPSA, another

measure of hydrophobicity.[64] Once we add our data, these measures are no longer fully

predictive of PDMS binding over the combined data set of 26 chemicals. We find that

insufficient hydrophobicity is still a useful predictor of chemicals that do not partition into

PDMS. Both LogP and TPSA can be used to establish such a threshold at less than 1.27 to

1.83 for LogP or greater than 70.2 to 76.2 Å^2 for TPSA. Note that these results were

obtained using unmodified PDMS; plasma treatments used to reduce PDMS surface

hydrophobicity could alter the LogP and TPSA binding thresholds.

Despite agreement on thresholds, we find that the degree of PDMS binding for chemicals

with LogP above (or TPSA below) threshold is no longer linearly related to TPSA. Neither

is it related to molecular weight (range from 187 to 808 g/mol) or polarizability (range

from 17 to 980 Å^3). Among those and 15 other molecular properties catalogued by

ChemSpider (http://www.chemspider.com), the best predictor of PDMS binding was LogP

above the noted threshold and the number of H-bond donor groups (T-test P-value =

0.0037). Highly hydrophobic compounds with no H-bond donor groups were strongly

sequestered by PDMS, those with one tended to be sequestered more modestly, and those

with two or more were affected weakly if at all. As demonstrated previously, diffusion through PDMS membranes is slower for chemicals with larger H-bond donor numbers,[102] and lower diffusivity in PDMS is associated with less sequestration in microfluidic devices.[92] Although LogP is a reasonable measure of how well a chemical partitions into PDMS versus aqueous solution,[103] this partitioning is only at equilibrium near the interface. Substantial loss of chemical from solution requires both surface partitioning and diffusion away from the surface. It is thus insightful, but not surprising, that the number of H-bond donors in a molecule can affect its sequestration by PDMS.

As shown in Figure 3-5, one notable exception to the above trend is rhodamine 6G. This compound has two H-bond donor groups, and yet Wang *et al.* concluded that it bound PDMS strongly.[63] When we tested rhodamine 6G in our experimental setup, we found a conflicting result with no measurable PDMS binding. Both setups were depletion experiments, i.e., measuring the amount of chemical left in bulk solution after some duration of exposure to PDMS, but the experiments differed in the method used to measure chemical concentration. Our experiments used UV-Vis absorption, whereas Wang *et al.* used fluorescence intensity. Fluorescence is more sensitive, but also subject to photobleaching or quenching, which could explain the discrepancy by yielding an apparent depletion of rhodamine 6G even in the absence of PDMS binding. We thus consider absorption spectroscopy a more robust measure of chemical concentration. Of note, rhodamine 6G was the only compound that Wang *et al.* quantified via fluorescence; the others were measured via radiolabels that are not subject to the same complications.[63]

Beyond elucidating the molecular properties that correlate with PDMS binding, our experiments quantify binding to PDMS in a way that provides new insights. First, for three of the five PDMS-binding chemicals tested here, the carrying capacity of PDMS exceeded 1000 molecules per nm^2. Such carrying capacities are obviously much too large to represent pure surface packing and it is well known that small molecules can diffuse into the PDMS bulk.[104] Building on the model presented by Shirure and George,[92] one would expect the carrying capacity to increase with a chemical's diffusivity within PDMS. Such diffusivity is however difficult to measure directly for non-fluorescent molecules. Carrying capacity thus provides an alternative and more easily measurable parameter for pharmacokinetic modelling that is valid at least over tens to hundreds of hours. This time regime is longer than the measured time constants associated with binding and desorption, which ranged from 2 to 18 hours.

These time constants are in a range that complicates the evaluation of multi-day chemical screening for targeted and/or adverse responses in microfluidically cultured cells and tissue constructs. Based on our modelling, the complications are three-fold. First, even if the nominal inlet concentration is constant, cellular exposure to a drug or potential toxicant will be time-dependent. Furthermore, the time needed to reach a steady-state exposure will be longer for lower inlet concentrations. Second, for chemicals that bind PDMS reversibly, even the steady-state cellular exposure will be less than the nominal dose – an order of magnitude less given the values we observe for the example of ethofumesate. Third, the delivery of acute doses of reversibly binding chemicals will be complicated by

long tails of extended low-dose exposure long after a bolus injection. Our modelling approach shows that these complications can be estimated and thus considered in evaluating cellular responses. It may also be possible to use this modelling approach in a reverse manner to design a time-dependent inlet concentration profile that yields a targeted time-dependent cellular exposure.

Conclusions

We have established a technique to measure chemicals' PDMS-binding kinetics and a method to use these measured kinetic parameters to model chemical transport in PDMS-based devices and thus predict time-dependent cellular exposures. Further, we have found that binding to PDMS is not only correlated with measures of hydrophobicity such as LogP or TPSA, but also increases for compounds with fewer hydrogen-bond donor groups. This finding can serve as an exclusion criterion for compounds likely to have strong interactions with PDMS and thus difficult to interpret effects on cells in PDMS-based devices.

Chapter 4

Experimental Methods and Theoretical Models

UV-Vis Absorption Spectroscopy

UV-Vis absorption spectroscopy was the primary technique used to measure the change in chemical concentration resulting from chemical partitioning into PDMS. One advantage of UV-Vis spectroscopy is the closed system created by sealing cuvettes with vacuum grease allows continuous, real-time measurement of chemical kinetics without intervention. Closing the chemical-PDMS system removes environmental effects such as light, heat, evaporation, or human contamination. Further, more complex measurements to quantify change in chemical concentration, such as fluorescence, are more likely to introduce error as they not only require absorption of a photon, but also add additional uncertainty in the measurement of the emitted light. For example, a decrease in fluorescence intensity could result from photobleaching.

From Beer's law, chemical absorbance (A) is proportional to molar extinction coefficient (ε), path length of light traveling through chemical solution in the cuvette (l), and molar concentration (c). Absorbance is also defined as the log ratio of incident light intensity to transmitted light intensity

$$A = \varepsilon l c \qquad \qquad (4\text{-}1).$$

$$A = log\frac{I_0}{I_t}$$

By maintaining a constant path length with matched cuvettes, the changing solution concentration can be determined after converting absorbance to concentration units using a calibration curve (Figure 4-1). Note that the Beer's Law relationship relies on the assumption that concentration dependence on absorbance peaks in the spectrum is linear over a certain range. The Varian Cary 5000 (Agilent, Santa Clara, CA) dual-beam UV-Vis absorption spectrometer setup allows a reference beam to simultaneously measure a cuvette filled with solvent in order to provide the initial beam intensity. The spectrometer automatically calculates the log ratio of transmitted intensities to output an absorbance

$$A = x \cdot c + b$$

Residual Sum	0.02258	
Pearson's r	0.99555	
Adj. R-Square	0.99043	
	Value	Standard Error
Intercept	-0.00593	0.01877
Slope	2.98706	0.07844
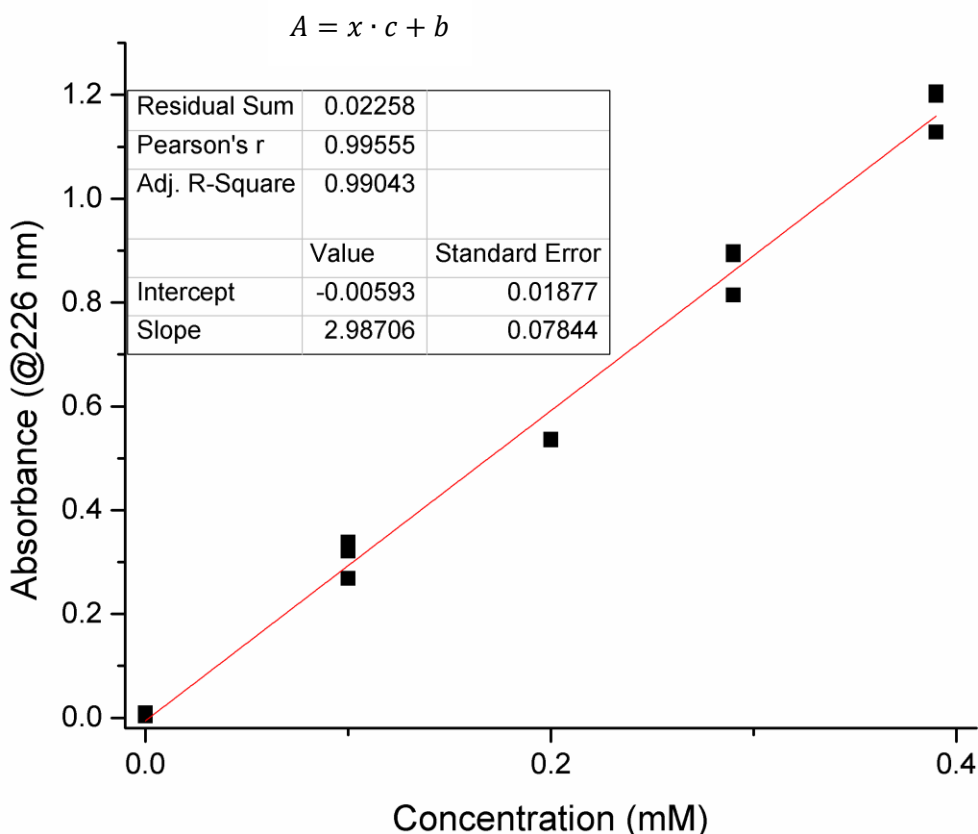
Figure 4-1: A typical calibration curve to convert peak absorbance to concentration with a linear conversion equation (inset). This calibration was used for propiconazole.

spectrum free of solvent contributions. For quantitative studies, the concentration should

be kept low enough to keep the absorbance less than one. A measured absorbance of 1.3,

for example would result in only 5% of light reaching the detector, greatly lowering the

signal-to-noise ratio. When consideration of signal noise is taken into account, the

maximum signal-to-noise ratio is found at an absorbance of 0.4[105]. A more detailed

protocol for UV-Vis puck soak experiments is presented here.

Chemical solutions were created by finding the experimental extinction coefficient and

using Beer's law to predict the concentration to achieve an absorbance of 1. The chemical

solution was mixed to the desired concentration by measuring either powder by weight or

liquid by volume. Viscous liquids were able to be measured by cutting the tip off a pipette

and carefully removing the desired volume to calculate the concentration from known

chemical density. Since many chemicals were hydrophobic, dilutions were performed in a

series of steps, starting with dissolving the chemical into pure DMSO with the aid of

sonication. Then, a series of three dilution steps followed each time diluting the DMSO

solution by an order of magnitude in PBS until a 0.1% DMSO concentration was reached at

the desired chemical solution concentration.   For hydrophilic chemicals (logP<1) this step

was not necessary and chemical was mixed into water aided by sonication in a single step.

PDMS was prepared by mixing a 10:1 ratio by weight of liquid elastomer to clearing agent.

The total amount of liquid should be ~5g more than the desired weight in order to account

for adhesion to the plastic mixing cup. The total weight of PDMS mixed depends on the

container, square well plates for example require 8 g/mm height and circle plates require 6

g/mm. The liquid PDMS was mixed with a centrifuge function of 2-mins of spinning and 2-mins of de-gas. After pouring into the well plate, the mixture is then placed in a vacuum to de-gas for at least 10 minutes and afterwards requires additional applied air pressure to remove air bubbles that ultimately rise to the surface. The liquid PDMS is then solidified in a pre-heated oven for at least 5 hours or overnight. A 5 mm diameter tissue punch was used to make the cylindrical disks. The easiest way to remove PDMS from the tissue punch is to poke through the top with a clean plastic pipette. Quartz cuvettes were used to hold solution to minimize UV absorbance in the cuvette walls. A matched pair of cuvettes were placed in the sample and reference beams of the spectrometer. The reference solution was the solvent used in chemical preparation and for a fresh batch of solvent, a blank measurement containing only solvent was measured to insure no trace of contaminants and that the solution was well-mixed. The important settings to specify for the spectrometer are the wavelength range of interest (all chemicals were first scanned from 200-800 nm and later narrowed to the peak of interest) and acquisition time which was selected to be as long as possible while still taking less than 10 minutes per spectra in order to maintain an adequate temporal resolution. No baseline corrections were used with the software, these were applied later (explained in the Spectral Subtraction section).

Although the closed PDMS-in-cuvette system works well for chemicals that bind strongly to PDMS, there are exceptions that require alternative methods. The use of the Nanodrop 2000c (Thermo-Fisher, Waltham, MA) UV-Vis spectrometer allows an analysis of microliter quantities of solution flowing through actual microchannels. This method allows for a

careful look at some chemicals that could weakly bind to PDMS in concentrations that would not be resolved in the small change in absorbance due to the cuvette volume being exposed to the much smaller disk surface. The Nanodrop absorption spectrometer relies on the same principle of absorbance in Equation 4-1, but introduces attenuated total internal reflection (ATR) to measure minute quantities of sample. Due to the quick attenuation of an evanescent wave, the signal can be confined to the surface concentration of interest.   The drawback of this method is the increased time of channel fabrication and experimental set-up that involves creating a channel for every time point. The detailed experimental protocol for channel measurements is detailed below.

The channel fabrication involves the same PDMS preparation steps with the exception that a silicon channel mold is placed at the bottom of the circular well plate before pouring. The first pour of this mold is used to measure and verify the channel dimensions using a light microscope with ocular reticule.   The channels are cut out of the circular well plate with the inner diameter cut at the edge of the channel leaving an outer edge of PDMS behind along with the mold remaining at the bottom. Subsequent pours to the mold are then filled to a 4 g/mm for a desired height which needs to be at least 3 mm tall for a structurally sound channel. Additional PDMS is cured without a mold in order to be the smooth sandwich layers pressure fit to the top and bottom closing the channel during experiments. Before the addition of chemical, channels are cut with a rounded scalpel in pairs and completed using a 1 mm diameter tissue punch to punch inlet and outlet reservoirs in the channel (an unfolded paperclip works well to remove PDMS from the punch). The pairs of

channels are then press-fit to a rectangular bottom piece of cut PDMS and chemical is pipetted into the inlet. A syringe is used to create a vacuum seal at the outlet and pull the solution through the channel. Chemical solution is added until the tops of the inlet and outlet are both filled. The channel is then sealed by press-fitting another cut piece of PDMS. Solution is removed from each channel by removing the top fitted piece of PDMS exposing the inlet and outlet and pipetting all solution from the outlet into a microcentrifuge tube. Then carefully using the syringe pressure to pull the rest of the solution into the empty outlet and pipetting again. This is repeated until the channel is empty and in the case of desorption experiments the channel is blown with nitrogen to insure to trace solution is left on the surface. A channel mold makes six well-formed channels at a time and thus channel experiments involved five time-points for adsorption experiments (a t=0 pipette straight to a microcentrifuge tube, the first three channels and the last adsorption time being pipetted from the last three channels as the near-saturation point) and three for desorption experiments. The Nanodrop spectrometer uses a 1 µl droplet on the surface of the ATR chip and first blanks the solvent solution. All timepoints were measured back-to-back to minimizee spectrometer drift.

Among the chemicals we tested, only perfluorooctanoic acid (PFOA) was unable to yield reliable absorbance measurements because its absorbance peak lies close to the UV detector edge. Therefore, another method of quantifying concentration was required for PFOA. The method we chose was ATR spectroscopy, which presents several advantages over simpler UV-Vis absorption spectroscopy.

ATR-FTIR Spectroscopy

As mentioned in the previous section, FTIR spectrum can be confined to the sample surface. Here, chemical binding was measured using the ATR attachment directly on the PDMS surface. This provides a direct measurement of the chemical concentration on the PDMS itself. The calculated penetration depth is expressed as

$$d = \frac{\lambda n_1}{2\pi \sqrt{sin^2\theta - (\frac{n_2}{n_1})^2}}$$

(4-2)

where λ is wavelength in air, n_1 and n_2 are the indices of refraction for the ATR crystal and sample, respectively, and θ is the angle of incidence at which light hits the sample-ATR
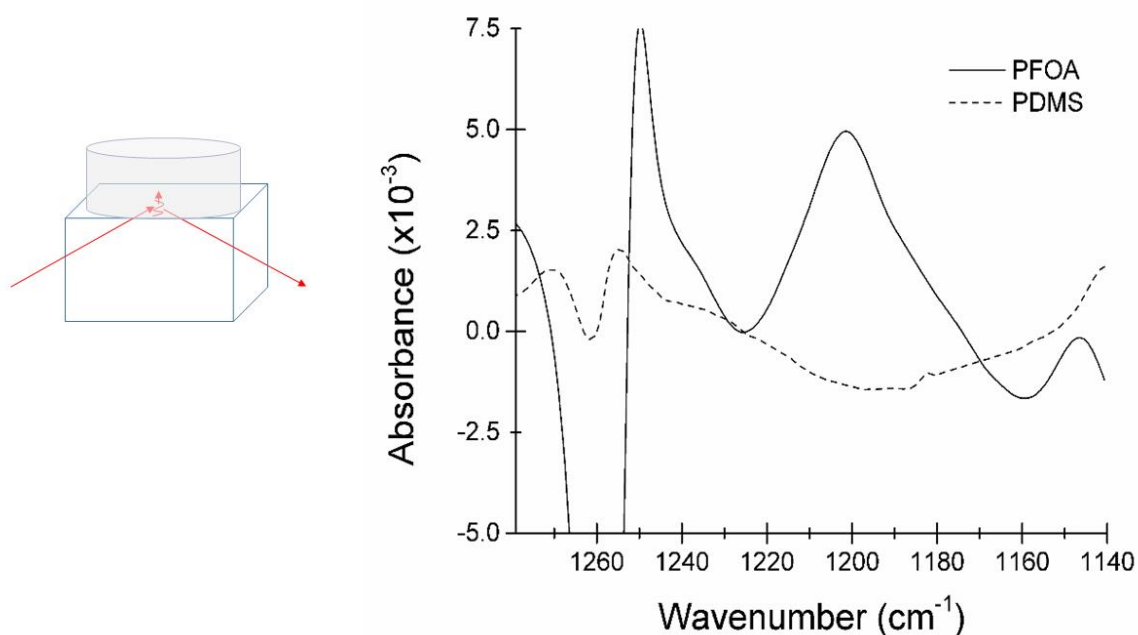
Figure 4-2: (Left) Experimental set-up for ATR-FTIR experiments. After soaking, disk was dried and placed directly on the diamond single-hit ATR for measurement. (Right) Mid-IR spectra of PFOA (solid line) and PDMS (dashed line). Note that there is very little vibrational activity from 1140-1260 cm^{-1}.

interface. Taking θ to be 45°, using the index of refraction for diamond and water, and estimating the wavelength of infrared light as 5 µm yields a penetration depth of ∼ 4 µm for our samples. Unlike UV-Vis spectroscopy, which measures electronic energy levels, FTIR spectroscopy provides different molecular information by measuring vibrational energy levels. As in UV-Vis spectroscopy, ATR-FTIR spectroscopy can measure chemical concentration by quantifying the height of a peak, which in this case corresponds to the strength of a molecular vibrational mode. The absorbance can then be converted to concentration by a calibration curve just like in Figure 4-1. One disadvantage of this technique is that many small molecules of interest do not have a strong dipole moment, rendering them IR inactive. The other drawback is that PDMS and water are both strongly IR active. For these reasons, most chemicals were not suitable for measurement with this technique. However, PFOA has strong vibrational bands that do not overlap with the PDMS substrate and yielded valid quantitative data. Figure 4-2 depicts the experimental setup and spectra of the PFOA experiment. More detail on the ATR-FTIR experimental protocol is presented below.

Soak experiments were done as for the disk-soak experiments of dual-beam UV-Vis absorption spectrometer except only one time point was taken. All soaks were done simultaneously with t=0 point taken just before being introduced to the cuvette. The cuvette was used here only to preserve the exact volume and conditions of the disk-soak UV-Vis experiment. The final soak timepoint was measured after the puck was blow dried with

nitrogen and placed flat against the ATR chip using light pressure from the ATR arm attachment.

Future substrates to replace PDMS with less mid-IR activity may give better prospects for ATR-FTIR analysis of chemical kinetics. ATR-FTIR was used to probe structural information including vibrational activity that may overlap with chemical detection if used as a future substrate (Figure 4-3). Future lab-on-chip device substrates such as SEBS with weaker
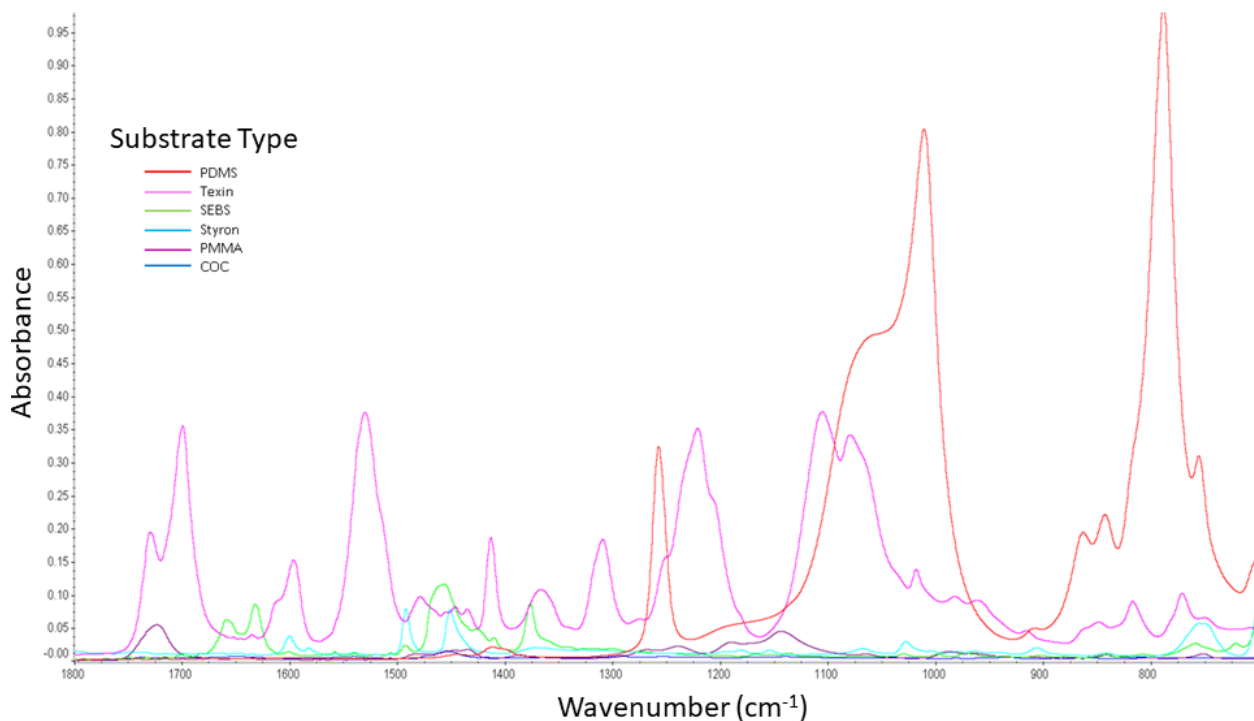
Figure 4-3: Comparison of ATR-FTIR spectra for different microfluidic device substrates. Spectra for ATR-FTIR experiments were averaged over 100 accumulations until reducing the noise threshold to less than 10^{-5}.

vibrational bands than PDMS in the 800-1500 cm^{-1} region of interest may allow for easier direct measurement of chemical binding by ATR-FTIR.

Spectral Background Subtraction Algorithm

In order to isolate the spectral peak of interest and to accurately measure the change in peak absorbance over time, the contributions of the solvent (in calibration experiments) or the PDMS substrate (in direct binding measurement of the PDMS surface) must be removed (Figure 4-4).
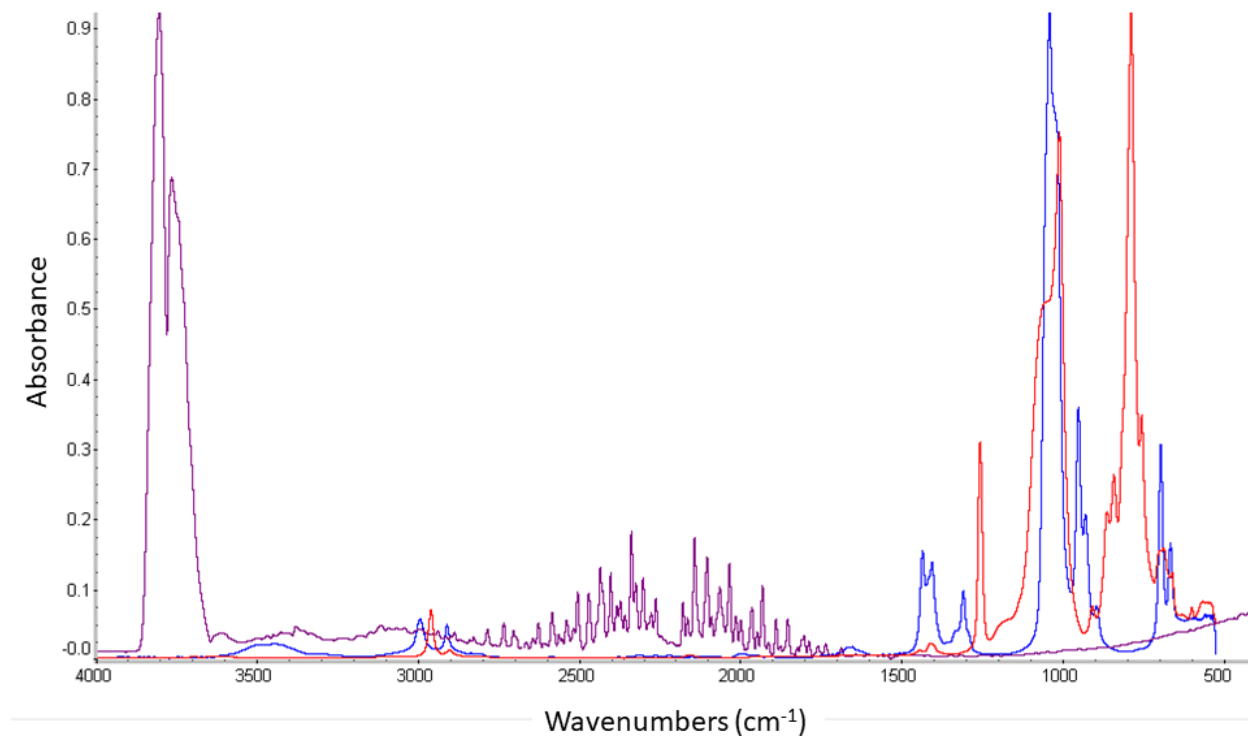
Figure 4-4: Spectra of common unwanted IR active molecules throughout entire FTIR vibrational window (800-4000 cm^{-1}). DMSO spectra (blue), PDMS substrate (Red), water vapor and CO_2 in the air (purple).

There exists proprietary software with built in methods of subtracting an unwanted solvent or substrate contribution for vibrational spectra such as OMNIC (Thermo Fisher, Waltham, MA). These algorithms are unreliable as they work in a "black box" and produced erratic peak variation. An alternative method to eliminate solvent contributions that avoids black-box proprietary software was minimization of mean square difference (MSD).

To subtract an unwanted spectral contribution, a wavenumber range is chosen $v_{min} < v < v_{max}$ that ideally contains a region where the solvent or substrate is vibrationally active, but does not contain activity from the chemical of interest. Chemicals must have solvent spectra provided as a separate file and then removed and shifted as close to zero as possible by an offset term. The algorithm subtracts the y-component of the spectra (for each ordered pair that makes up the total) from the pure solvent. The algorithm calculates the square difference absorbance for each wavenumber (v), which is the absorbance (A) from the sample spectra minus the solvent absorbance (A_s) multiplied by a constant α and an offset c. The mean square difference (MSD) is then calculated by summing over the square difference at each wavelength. The algorithm then finds the values of $\bar{\alpha}$ and c that minimize the mean square difference (MSD) absorbance for all wavelengths in the region of interest $v_{min} < v < v_{max}$

$$f(v, (A - \alpha A_s - c)^2) = f(v, MSD)$$

$$MSD = \sum_{i=1}^{n}(A_i - \alpha A_{i,s} - c)^2 \qquad (4\text{-}3).$$

$$for \ v_{min} < v < v_{max}$$

The offset term, c, is necessary in this situation since we only want to weight subtraction by the relative difference of solvent and sample contributions in a region and don't want to artificially manipulate the spectra to approach a MSD of zero. An example is a difference spectra, where two similarly sized peaks should ideally subtract to make a flat line. However, in the case where these two peaks are slightly shifted in the solvent and sample spectra over subtraction could occur. This would result in a smaller MSD in that region, but could also produce in over subtraction in other spectral regions of interest. The difference minimization only works well for peaks that are well-aligned and several orders of magnitude above the noise threshold. The spectral subtraction is then iterated again in order to apply an offset to correct for changes in baseline alone

$$f(v, (A - c)^2) = f(v, MSD)$$

$$MSD = \sum_{i=1}^{n}(A_i - c)^2 \qquad\qquad (4\text{-}4).$$

$$for\ v_{min} < i < v_{max}$$

Here, v_{min} and v_{max} may be modified to select a region of lowest vibrational activity adjacent to the peak of interest. The latter baseline offset algorithm is used for UV-VIS spectra, whereas both are used for ATR-FTIR spectra. Unfortunately, subtraction of water vapor from the vibrational spectrum is not successful in this case. This is due to the difficulty of obtaining a water vapor spectrum that is close enough to its contributions in the sample spectrum while also remaining above the noise level and is unshifted due to temperature.

Pseudo 1st Order Binding Kinetics (Macroscopic Model)

After spectroscopic measurement and processing (baseline subtraction and absorbance to concentration conversion) data is fit to a model of chemical binding in order to extract relevant rate constants for analysis.   To accomplish this, a pseudo 1st order model of binding kinetics is useful for a first pass empirical fit. In this model, a chemical solution of known initial concentration is added to a substrate with a fixed number of binding sites. This simple reaction can proceed in two ways: an irreversible or reversible reaction. For the case where chemical binding to a binding site is irreversible, we can write the reaction as

$$[A] + [S] \rightarrow [AS] \qquad\qquad (4\text{-}5).$$

Where A is the chemical concentration in solution, S is the free surface site concentration, and AS is the concentration of bound sites.

In a chemical reaction between a ligand (chemical binder) and a receptor site, from the Law of Mass Action the rate of forward reaction can be written as a function of the chemical concentration in solution, the concentration of free surface sites and a forward rate constant with units ($M^{-1}hr^{-1}$):

$$\alpha \frac{78}{dt} - -k_f[A][S] \qquad\qquad (4\text{-}6)$$

where the subscript (1) denotes the concentration in the forward reaction, α is the ratio of the volume of chemical solution to the exposed surface area of PDMS. At t=0, the receptor and chemical concentrations can be rewritten as

$$\alpha \frac{dA_1}{dt} = -k_f A_0 S_0 \qquad (4\text{-}7).$$

where [S] is S_0, the binding site density of PDMS, [A] becomes the starting chemical

concentration A_0.

Combining Equation 4-7 and Equation 3-1 from the empirical fit of experimental data in

Chapter 2, we can solve for the forward rate constant:

$$k_f = -\frac{\alpha \Delta A_1}{\tau_1 A_0 S_0} \qquad (4\text{-}8).$$

In the reverse reaction experiment, the binding sites are introduced to a solvent that

initially contains no chemical concentration, and over time the reaction proceeds

backwards by a reverse rate constant k_r. The reversible reaction can be written as

$$[A] + [S] \leftrightarrow [AS]$$

$$\frac{dA_2}{dt} = k_r[AS] \qquad (4\text{-}9).$$

t=0 of the reverse reaction experiment starts with all sites bound, and Equation 4-9

becomes

$$\frac{dA_2}{dt} = k_r \Delta A_1 \qquad (4\text{-}10).$$

Plugging in Equation 3-2 from the empirical fits in Chapter 2 to Equation 4-10, we can solve

for the reverse rate constant

$$k_r = \frac{\overset{72}{\Delta A_1}}{\Delta A_2 \tau_2} \qquad (4\text{-}11).$$

77

The on and off rates are equal at equilibrium, thus

$$k_f[A][S] = k_r[AS]$$

$$k_f A_\infty (S_0 - \Delta A_1 \alpha) = k_r \Delta A_2 \alpha \qquad (4\text{-}12).$$

Combining Equations 4-8, 4-11 and 4-12 and solving for the forward rate constant and surface site density gives working Equations 4-13 and 4-14:

$$k_f = \frac{1}{\tau_1 A_0} - \frac{\Delta A_1}{\Delta A_2 \tau_2 A_\infty} \qquad (4\text{-}13);$$

$$S_0 = \frac{\alpha \Delta A_1^2 \tau_2 A_\infty}{\Delta A_1 \tau_2 A_\infty - \tau_1 A_0 \Delta A_2} \qquad (4\text{-}14).$$

For the irreversible case, $\Delta A_2 = 0$, $and\ \tau_2 \to \infty$, $S_0 = \alpha \Delta A_1$ and $k_f = \frac{1}{\tau_1 A_0}$. A true irreversible reaction is not taking place in this experiment, but rather $k_f \gg k_r$. This means that S_0 is actually a measure of the equilibrium binding site density. For irreversible binding, S_0 is very close to the maximum binding site density.

Microscopic Model

The more sophisticated microscopic model was developed in order to simultaneously fit the forward and reverse reaction from the same spectroscopic data empirically fit in the previous section. In the pseudo 1st order model, Equation 4-9 was approximated by separate estimated empirical fits to the forward and reverse reactions. The issue with this method is that both forward and reverse reactions are taking place in both sets of experimental data, so an empirical fit neglects the reverse rate constant in the adsorption experiment, and vice-versa. The exact differential equation representation of Equation 4-9 is

$$\frac{dA(t)}{dt} = -k_F A(t)\left(\frac{S_0}{\alpha} - \left(A_{tot} - A(t)\right)\right) + k_R(A_{tot} - A(t)) \qquad \text{(4-15).}$$

For irreversible binding we can assume $k_f \gg k_r$ which causes the left side of Equation 4-15

to dominate allowing a simplification to

$$\frac{dA(t)}{dt} = -k_F A(t)\left(\frac{S_0}{\alpha} - \left(A_{tot} - A(t)\right)\right) \qquad \text{(4-16).}$$

Both cases can be solved analytically.

The two simultaneous solutions to Equation 4-15 are

$$A_1(t) = -\frac{1}{2k_f\alpha}\big(k_r\alpha + k_f(S_0 - A_0\alpha) +$$

$$\sqrt{-k_r^2\alpha^2 - k_f^2(S_0 - A_0\alpha)^2 - 2k_r k_f \alpha(S_0 + A_0\alpha)}\tan\Big(\frac{t\sqrt{-k_f^2 S_0^2 + 2k_f(-k_r + A_0 k_f)S_0\alpha - (k_r + A_0 k_f)^2\alpha^2}}{2\alpha} -$$

$$\tan^{-1}\Big(\frac{k_f S_0 + k_r\alpha + A_0 k_f\alpha}{\sqrt{-k_r^2\alpha^2 - k_f^2(S_0 - A_0\alpha)^2 - 2k_r k_f\alpha(S_0 + A_0\alpha)}}\Big) \qquad \text{(4-17a);}$$

$$A_2(t) = -\frac{1}{2k_f\alpha}\big(k_r\alpha + k_f\big(S_0 - A_0\alpha + A_1(t)\big)$$

$$+ \sqrt{-k_r^2\alpha^2 - k_f^2\big(S_0 - A_0\alpha + A_1(t)\big)^2 - 2k_r k_f\alpha\big(S_0 + A_0\alpha - A_1(t)\big)} \cdot$$

$$\tan\Big(\frac{t\sqrt{-k_r^2\alpha^2 - k_f^2\big(S_0 - A_0\alpha + A_1(t)\big)^2 - 2k_r k_f\alpha\big(S_0 + A_0\alpha - A_1(t)\big)}}{2\alpha} -$$

$$\tan^{-1}\left(\frac{k_r\alpha + k_f\big(\alpha A_0 + S_0 + A_1(t)\big)}{\sqrt{-k_r^2\alpha^2 - k_f^2\big(S_0 - A_0\alpha + A_1(t)\big)^2 - 2k_r k_f\alpha\big(S_0 + A_0\alpha - A_1(t)\big)}}\right) \qquad \text{(4-17b)}$$

For the irreversible case, $k_r=0$ can be plugged into the Equation 4-17a, which then reduces

to

$$A_1(t) = -\frac{S_0 - A_0\alpha}{2\alpha} + \sqrt{-k_f^2(S_0 - A_0\alpha)^2}\tan(\frac{t\sqrt{-k_f^2 S_0^2 + 2A_0 k_f^2 S_0\alpha - (A_0 k_f)^2\alpha^2}}{2\alpha} - tan^{-1}(\frac{k_f S_0 + A_0 k_f\alpha}{\sqrt{-k_f^2(S_0 - A_0\alpha)^2}})) \qquad (4\text{-}18).$$

Confocal Microscopy

Fluorescently tagged Drosophila epithelial cells were imaged by a Zeiss LSM confocal

microscope and Spinning Disk Confocal microscope. Confocal fluorescent images were

used to determine the triple junction orientation angles for tension analysis in Chapter 2.

Confocal microscopy works by combining fluorescence imaging by laser excitation and

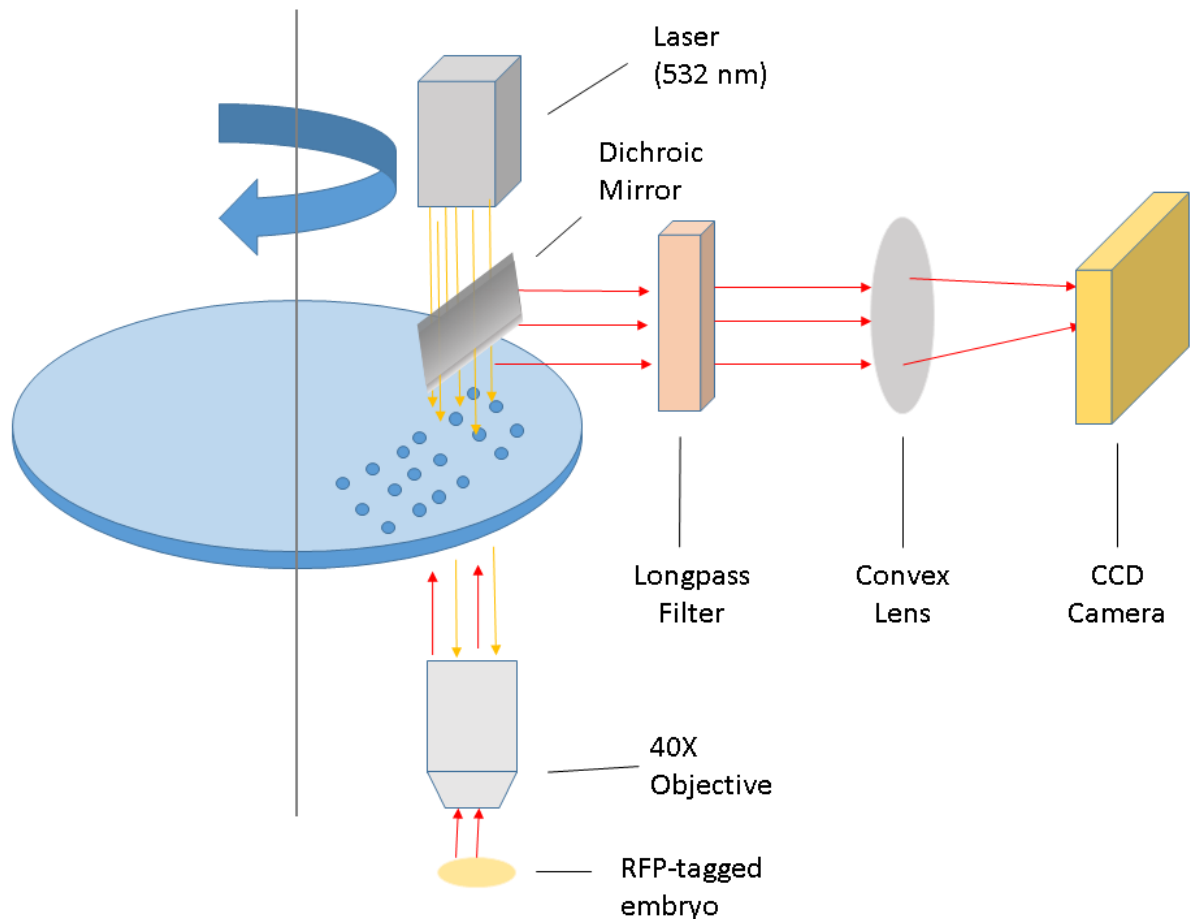Figure 4-5: Cartoon of spinning disk confocal microscope. The collimated laser excitation light (orange) enters the pinhole-filled rotating disk and illuminates many spots on the sample simultaneously. The fluorescent light (red) can only re-enter through the disk pinholes if it is within the depth of focus. The fluorescence is then reflected by a dichroic mirror and is filtered and focused onto a CCD.

isolating the depth of field using a pinhole. The setup of a typical spinning disk confocal microscope is shown in Figure 4-5.

In the case of laser scanning confocal microscopy, a laser is raster scanned across a sample, and the image is formed one pixel at a time detected by a PMT. The problem with this is that the speed of imaging is limited by the laser raster speed. Spinning disk microscopes use a collection of hundreds of pinholes spun so quickly that the laser rapidly illuminates the entire sample, which is recorded with powerful EMCCD cameras. The key to quickly imaging multiple samples is to switch between the brightfield illumination and fluorescence microscope. Embryos should be located and roughly staged using brightfield illumination with a 40X magnification providing sufficient resolution to view the amnioserosa. Embryos with granules dispersed throughout the embryo (instead of contained in the visible yolk sac) or an epithelium that contains only patches of visible cells can be seen under brightfield and are likely dead. Like-wise ventral facing embryos are easily identified by their shape and distinct lack of amnioserosa. The locations of embryos of interest are marked on a separate brightfield image of the entire slide under 5X magnification to assist with proper orientation and repeat imaging. Once embryos are identified and roughly staged then they can be fluorescently imaged. Fluorescent imaging is important to leave as the last step because prolonged exposure to laser light will cause unnecessary damage through photobleaching. However, photobleaching is a greater concern in live imaging than fixed and stained embryos which have photobleaching protection built-in.

The reduced field of view associated with spinning disk measurement was too small to image *Drosophila* in a single image, instead requiring automated stage adjustment to take six images that would later be stitched together using an ImageJ software plugin.

SeedWater Segmenter

In order to analyze germ band triple junction angles and cell aspect ratios, a stitched fluorescent image obtained in the previous section needs to be converted to an accurate outline of the cells. SeedWater segmenter is a GUI created by former student, David Mashburn, that maps cell borders (segmentation) and assigns cell IDs to a fluorescent microscope image[28]. SeedWater uses a watershed algorithm which works by filling cells from a selected pixel (seed) from darkest pixel first slowly raising the "water" level until regions meet at the brightest intensity found at cell boundaries[57]. In order to best perform segmentation, it is useful to have an organized pipeline of processing steps. First, a folder for each imaged embryo segment is created that contains a composite image of several frames of neighboring segment stitched together. The imaged segment from each time point is given a new folder in order to carefully catalog SeedWater output. The goal of Seedwater is for each seed of the watershed to be placed inside a separate cell of interest and for all cells to have a seed, excluding cells whose fluorescent boundaries are incomplete or directly border the edge of the tissue, segment, or 2D imaging plane. Once seeds are placed, the algorithm typically fills cell interiors and marks cell borders accurately; however, manual user intervention is sometimes required. Verifying that each cell's borders are correct may require removing or repositioning a seed to better weight a border in the case of a dimly marked border. Specifically, it is often best to place the seeds

82

of two ill-defined neighboring cells as close to their border as possible. The borders of the segments themselves are often roughly defined, so the draw tool can be used by connecting a continuous line around the entire segment as close to the fluorescently marked cell borders as possible. The draw tool is powerful as it can remove artificially large cells by placing a manual boundary that shrinks the cell back to its correct shape.

Once saved, a CVDGenerator.py file converts the segmented output file to a list of triple junction angles and locations. It is useful to run this Python script while keeping the SeedWater window open, since some of the previously mentioned problems can produce a "degeneracy error" that requires further inspection of the watershed. Some common errors that lead to "degeneracy error" are cells that are too small in area, cells that are too large in area (the color map identifies these errors), cells with extremely rugged boundaries, cells that don't come together in what could be approximated as a triple junction, and cells that are isolated (i.e., cells must be bordered by at least three other cells). Finally, these conditions are affected by the fact a line segment drawn between triple junctions in the CVDGenerator is by default set to a straight line segment between two endpoints. When introducing an additional point to define the segment, the rough cell boundaries are more relaxed and CVDGenerator.py does not encounter errors; however, this leads to many errors in triple junction angle calculations in β-θ analysis. The minimum number of cells required for an accurate analysis is ~20, but it is better to be selective and exclude problem cells while adhering to a simple cell outline scheme.
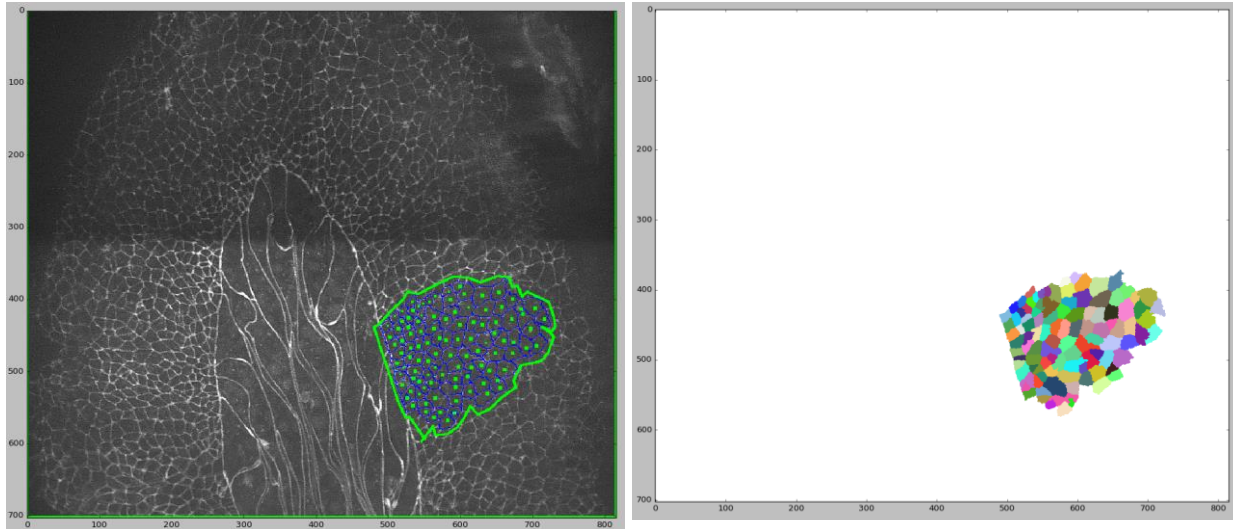
Figure 4-6: SeedWater segmenter screenshots showing the segmenting of A6. (Left) Seed view—working view to place seeds and draw green border to remove extraneous cells. (Right) Watershed view—shows filled in cells to check for any isolated or oddly shaped before converting to many nodes and edges.

Drosophila Genetics and Embryo Preparation

Hindsight (*hnt*) mutant embryos were created by crossing a fluorescently tagged balancer with heterozygous *hnt* positive mutants. The purpose of this cross was to positively identify *hnt* mutants as embryos at a stage before lethality. *hnt* is located on the x-chromosome and is homozygous lethal in embryos after germ band retraction. Thus, males are capable of single copy expression of *hnt,* but there is no physically observable difference between male and female *Drosophila* embryos. The genetic cross shown in Figure 4-7 below illustrates a method to fluorescently label non-homozygous females and non-*hnt* males using a balancer. Transgenes of interest can be genetically stabilized and passed down through generations without having to continuously repeat crosses because of genetic balancers unique to *Drosophila*. Balancers are scrambled sequences of DNA associated with a particular chromosome that have dominant genotypes, correspond to

84

easily observed phenotypes, and are homozygous lethal. In other words, an embryo cannot

be formed that contains a balancer copy passed down from both parents. This means any

transgenes paired with a balancer on the same chromosome can theoretically be conserved

from one generation to the next leading to simplified genetic crosses to achieve phenotypes

of interest for imaging studies. The ability to use balancers to efficiently incorporate

genetic mutations into the Drosophila genome makes it an attractive model system. In the

notation of Figure 4-7, each line is a new generation, with the cross beginning with the

$$\text{F0} \qquad \frac{Fm7RFP}{y} \ X \ \frac{Hnt}{Fm7}$$

$$\text{F1} \qquad \frac{Hnt}{Fm7RFP} \ X \ \frac{Fm7RFP}{y}$$

$$\text{F2} \qquad \frac{Fm7RFP}{Fm7RFP}, \quad \frac{Hnt}{Fm7RFP}, \quad \frac{Fm7RFP}{y}, \quad \boxed{\frac{Hnt}{y}}$$
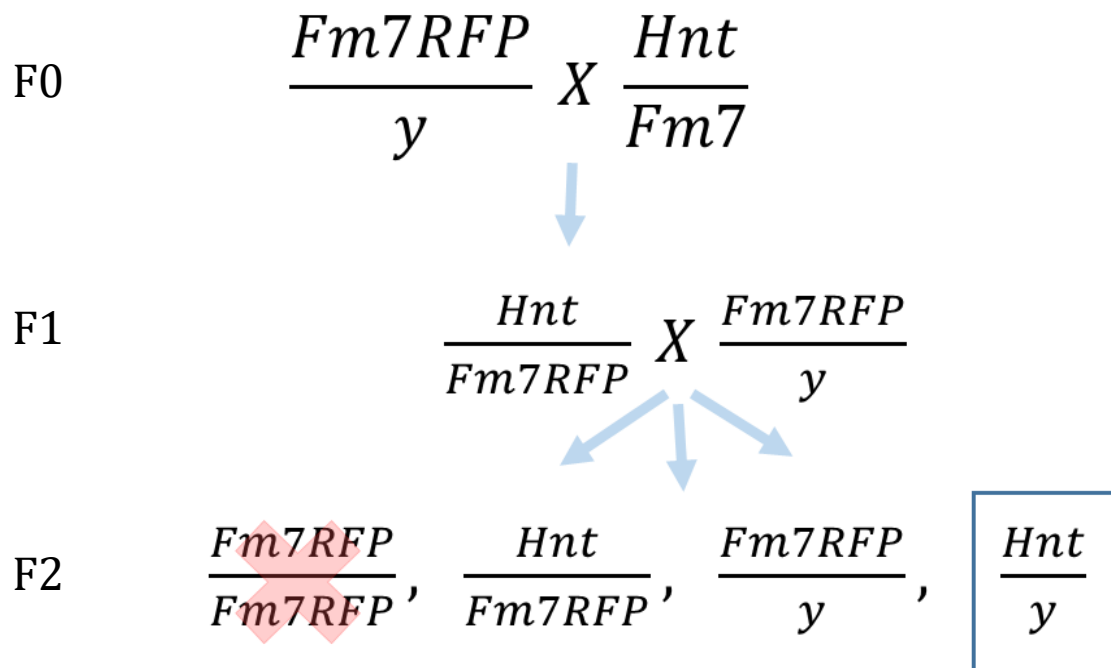
Figure 4-7: Mendelein genetic cross to combine *hindsight* (hnt) embryos with RFP
tagged balancer. Male chromosome is denoted by (y), and Fm7 stands for first
chromosome and the location of the balancer. The final generation F2 results in four
possible offspring including the desired *Hnt/y* embryos. *Fm7RFP* homozygous flies are
crossed out due to this genetic combination being embryonic lethal and hence not a
possible embryo outcome.

parent strand at F0.   A fraction indicates genes at different locations on the same chromosome. Commas separate different possible outcomes (all of equal probability in a strictly Mendelein model) from mating parents in the previous generation. A more detailed protocol of the *Drosophila* cross follows.

In order to cross two adult mutants, a male of suitable phenotype is selected. To accomplish this, flies are anesthetized with CO_2 while being examined under a dissecting microscope. Male fly anatomy is distinguishable from female primarily by their dark, rounded genitalia compared to females rounder pointed genitalia. Female flies are also larger and pre-pubescent females have an engorged abdomen. For the selection of F0 males for example, flies would be chosen with dark genitalia, bar-shaped eyes and the RFP expression could also additionally be verified under a widefield fluorescent microscope in the abdominal region. Female flies selected for a cross must be virgins to avoid fertilization from unknown males. Virgin females are identifiable by their expanded abdominal shape and the presence of a dark meconium stain on the abdomen. The ideal ratio of females to males to be isolated in a cross is 2:1. It is also important to provide extra dry yeast, as well-fed flies are more likely to mate.

 To collect embryos, yeast is added to a grape gel-plate on top of a collection vial. Collection timing is essential for accurate experimental results. To collect a sufficient number of embryos, the grape gel-plate must be left on for at least one hour prior to collection in order to clear any mature embryos being held inside female flies. A new plate is then placed for collection of fresh embryos for another hour. Because embryos are laid during

this entire period the best temporal resolution in a fixed embryo experiment is ±1 hour which can shift results accordingly. Yeast consistency is extremely important when collecting large numbers of embryos. Active dry yeast is mixed with equal volume water and stirred vigorously. The yeast paste is viable for up to 48 hours, or until the paste becomes noticeably dry. 24-48 hours before collection, embryos should remain in their stock bottle and a large amount of yeast paste should be added to the sides of the bottle as well as the food at the bottom. Flies that are well-fed before collection produce large numbers of embryos laid promptly when vial collection commences. Stock bottles must be maintained carefully so the acidity of the fly waste does not liquefy the food at the bottom of the bottles, thus killing the flies. If liquification at the bottom of a bottle is suspected and flies are still alive, a piece of tissue paper can be inserted to attempt to soak up the liquid surface before removing flies. After collection, the developmental state can be controlled by reducing the temperature of the surrounding environment. The rate that decreasing temperature slows development is specified in Kuntz *et al.*[106].

Once embryos are collected, there are additional preparation steps before imaging. Dechorionation of embryos is required for microscopic imaging due to the waxy nature of the eggshell (chorion) that impedes quality imaging. Before dechorionation, the embryos are washed by constructing a tower of a stacked coarse and fine mesh filter to catch the embryos. Dechorionation is accomplished using bleach with two different methods. The first is using a glass tube to hold the embryos in a bleach solution and empty them onto filter paper. This method is useful for small numbers of embryos where mistakes in bleaching time can be corrected by manually rolling the chorion off with a toothpick. The

filter paper with the collected embryos can be placed directly onto a well plate filled with an agarose gel mixture lightly pressed to transfer embryos. For staining preparation, the number of embryos involved renders this method prohibitive. For large numbers, bleach concentration is increased to 60:40 bleach to DI water, and embryos are actively stirred in a beaker until they begin to clump together (a sign of chorion deterioration).

For fixing and staining, the dechorionated embryos are transferred with a paintbrush to a heptane solution. Methanol is then added and the vial is rapidly shaken in order to remove the vitellin membrane. The embryos are then transferred to a formaldehyde solution to complete the fixing process. Staining for this work involved the use of primary and secondary antibodies. The primary antibody targets and binds to proteins localized to the imaging region of interest. Several primary antibodies (armadillo, α-spectrin, 1B1) were compared as cell border markers with α-spectrin providing the best contrast. A secondary antibody with an attached fluorescent protein is then chosen from the same animal species to bind to the primary antibody. Each of the antibodies are introduced in the presence of a blocking solution containing bovine serum albumin which provides a cocktail of proteins to prevent non-specific antibody binding. The final step involves transferring embryos to Vectashield™ solution which provides a viscous media to mount embryos to a glass slide as well as photobleach protection.

To prepare slides for timelapse imaging of normal germ band retraction, embryos are aligned in parallel rows ventral side up on grape plates by being rolled with a toothpick. This is easily accomplished using the natural curvature of embryos as a guide. A solution of

"fly glue" is created by soaking pieces of double-sided scotch tape in heptane, which dissolves the adhesive into the heptane solution. When applied to a cover slip, the heptane evaporates leaving a surface covered in adhesive. The embryos in a row(s) are cut out of the grape plate in a rectangle with a scalpel and the cover slip is brought down aligning the "fly glue" region with the embryos, applying pressure until slightly deforming them and then lifting the entire row of embryos in one motion. For long term imaging (>2hrs), two strips of wet filter paper can be taped under a gas permeable membrane to prevent embryo desiccation and subsequent death.

Chapter 5

Conclusions and Future Directions

Chapter 2 addressed how to quantify a genetic defect that alters germ band mechanics during embryonic development. Understanding mechanical forces in the germ band is the first step towards recognizing how changes in tension in the ectoderm can modify *Drosophila* embryogenesis. Chapter 3 analyzed the kinetics of chemical binding to PDMS. This analysis has broad application to kinetics of a variety of chemicals and materials. The hope of this work is that better quantitative modelling from a physical perspective in both tissue mechanics and chemical kinetics will lead to advances in the fields of developmental biology and lab-on-chip engineering, respectively.

Conclusions

β-θ Analysis of Normal and Mutant Embryos

β-θ analysis provided valuable insight into germ band mechanics during retraction. Regardless of the segment or time point during retraction, the internal polarization is always oriented perpendicular to the axis of elongation. This reinforced the hypothesis originally suggested by Lynch *et al.* that internal polarization perpendicular to external stress act like eccentric contraction in muscles—facilitating stable elongation[11,12]. Tension anisotropy through β-θ analysis has been validated in germ band retraction by comparable results seen from laser ablation[12]. β-θ analysis also revealed that both wild-type and *hnt* embryos fixed and stained immediately after the conclusion of germ band retraction retained this perpendicular force anisotropy orientation even during dorsal closure. The

90

hnt results point to the strong possibility that the germ band has an intrinsic mechanism to maintain internal polarization, similar to a continuously contracted muscle.

PDMS Sorption in Microfluidic Devices

Several experimental approaches were used to investigate the degree of partitioning into PDMS for chemicals of different hydrophobicity. ATR-FTIR was useful for molecules that did not exhibit strong electronic absorbance in the UV-Vis range, or in the case of PFOA, had a peak too close to the detector edge. The other advantage was the ability to directly probe the PDMS surface for chemical measurements, rather than measuring indirect loss from solution. The disadvantage of ATR-FTIR was the strong PDMS vibrational bands that overlapped with many of the weaker bands possessed by a majority of the chemicals of interest. It would also require a time series experiment involving separate PDMS chemical soaks for each time point in order to extract rate constants.

On the contrary, UV-Vis absorption spectroscopy coupled with a dual-beam spectrometer was the most convenient technique. This set-up allowed multiple real-time PDMS soak experimental measurements. PDMS was sealed inside cuvettes for these experiments to minimize interaction with the outside environment while the soak was taking place. This method was very efficient at running time series experiments for multiple chemicals in parallel; however, it was not sensitive enough to detect incremental changes in concentration from weak binding chemicals. Small changes to concentration were undetectable due to the solution volume being much larger than available PDMS surface area. Fortunately, the concentration changes in weak binding chemicals could be detected

by Nanodrop UV-Vis absorption spectroscopy if chemical binding was measured in microfluidic channels. The channels had a large surface area to volume ratio and the channel geometry was very close to that of actual lab-on-chip devices. However, one disadvantage is that the channel solution volume was too small to use in a dual beam spectrometer. Chemical binding had to be measured with Nanodrop spectrometer that was more prone to instrument noise and required 10x the concentration to detect a change in absorbance due to its shorter pathlength. Additionally, each time point in a channel time series experiment required a separate channel fabrication and soak, rendering it time prohibitive when collecting extensive chemical data.

Determining which method to use, required predictive knowledge of the degree a chemical might bind to PDMS based on chemical properties. The two properties that were correlated with PDMS binding were logP and H-bond donor number. Using these two properties and experimental binding data, it was shown that logP below a threshold (<1.7) resulted in no binding to PDMS. Even chemicals with logP >1.7 did not bind PDMS if they also had >2 H-bond donors. Chemicals close to the aforementioned logP threshold were found to have weak partitioning into PDMS.

Overall, the best course for experimentally measuring binding of an unknown chemical was to look at its logP and H-bond donor number and determine if those numbers were near the binding threshold. Chemicals close to threshold needed to be measured using a microfluidic channel set-up likely due to the smaller changes in solution concentration

from weaker binding to PDMS. More hydrophobic chemicals could be measured with the straight-forward disk method.

Data from both the channel and disk methods of experimental binding were successfully combined to extract rate constants important for building a computational fluid dynamic model of chemical binding. This was verified for BPA, a chemical whose binding was able to be measured using both techniques. This is because BPA is more water soluble than other PDMS binders and the concentration could be adjusted to meet each spectrometers' sensitivity.

The experimental rate constants were successfully implemented into a computational fluid dynamic model using realistic device geometries to predict the cell chamber dose in a device for both bolus and continuous chemical injection. The results of this model revealed that strong binders lost up to an order of magnitude of their injection concentration into PDMS. This loss will need to be compensated for in future studies in order to establish accurate dose information. Additionally, some chemicals bound to PDMS reversibly and continued to desorb over the course of 48-hours. Thus, reversible binding chemicals cannot be used in a true bolus experiment. Any input bolus will be distorted by binding to and later desorption from PDMS channel surfaces.

Future Directions

β-θ Analysis

The analysis of germ band retraction in early dorsal closure in fixed embryos introduced

two unexplained phenomena: the cause of the large variability in internal polarization and

the inconsistency observed in the aspect ratio. There are two ways to investigate these

inconsistencies. The first would be to image both live Ecad-GFP and *hnt*;Ecad-GFP

embryos, in a manner similar to the normal germ band analysis. Imaging would now start

from mid-retraction all the way to early dorsal closure and analyze the internal

polarization to see if the variability persists. Live imaging would provide more sensitive

temporal resolution than embryos fixed at additional time points. Further, the temporal

resolution of analysis for a fixed embryo is limited by the hour-long collection time that

could introduce significant variability in internal polarization. Live imaging would allow a

more accurate staging by providing more temporal context rather than a snap-shot in time

to properly stage the embryo. It would also avoid needing large numbers of embryos due

to the ability to more easily manipulate a live embryo's orientation before mounting on a

slide. However, the cross for creating *hnt*;Ecad-GFP mutants would be a difficult cross due

to the need to have homozygous Ecad-GFP on both male and female flies in F1 of Figure 4-

7. The more mutations added on, the more sickly the fly becomes. Ecad-GFP and *hnt*, in

particular, drastically reduce embryo viability. Fixed and stained embryos could avoid this

complication with the addition of a working fluorescent balancer shown in Figure 4-7. The

drawback of this process is that fixing and staining is time consuming, requires large

numbers of adult flies to get enough progeny to fix and could create artificial results in the

94

fixation process which could influence cell geometry. Until the results of live imaged embryos are obtained for early dorsal closure, it will be difficult to ascertain whether the variability is artificial (a product of the fixation process) or of a morphological origin. The latter of which would further elucidate the internal mechanism of the germ band during dorsal closure. Additionally, β-θ analysis could be used to investigate other developmental time points as well.

Preceding retraction, the mechanics of germ band extension have been well studied[107–109]. During extension, the germ band undergoes cell shape change as well as intercalation. It has been found that while shape change has a stronger contribution in the first 30 minutes of extension, cell rearrangement then becomes the dominant effect[107]. β-θ analysis for germ band extension has the potential to confirm the claim that new junctions are formed between cells strongly polarized in the direction of extension resulting in a contraction akin to concentric contraction in muscles and that external stress from the midgut seen in ablation studies is oriented along the same direction[108]. These results indicate external stress and internal polarization can interact to produce different context-dependent movement. β-θ analysis can complement ablation experiment results for germ band extension, as it has with retraction. β-θ analysis has the potential to smoothly connect differences in tension in the germ band throughout multiple stages in embryogenesis to create a continuous model of tissue tension over time.

Despite showing no significant mechanical difference from wild-type embryos, *hnt* embryos fail to complete germ band retraction. Lamka *et al.* sought to rescue germ band retraction in *hnt* embryos using an H99 Deficiency double mutant that would prevent *reaper*-mediated apoptosis in the amnioserosa[8]. Despite the presence of the amnioserosa, retraction still failed[8]. The deficiency double mutant combined with an *hnt* line was unable to be produced by the genetic cross illustrated in Figure 5-1.

Further, male *Drosophila* of both stocks (particularly deficiency mutants) were sickly and became sterile when Fm7 balancer was combined with deficiency stock; thus, the deficiency side of the cross failed. This experiment needs to be verified by repeated imaging with cell border markers that were not used in the previous study to investigate how the deficiency mutant could have affected the *hnt* germ band. It is entirely possible that the hnt;DfH99 double mutant investigated in Lamka *et al.* represents a third germ band phenotype, mechanically altered from wild-type germ band, that is responsible for the failure to retract even in the presence of the amnioserosa.

$$\frac{Hnt}{Fm7RFP}; \frac{+}{Tm3aGFP} \quad X \quad \frac{Fm7RFP}{y}; \frac{Df}{Tm6B}$$

Figure 5-1: Genetic cross to create *Hnt*;H99 deficiency (*Df*) double mutant. Semi-colon represents genes on separate chromosomes. Three balancers are used: bar shaped eyes on the first chromosome with ubiquitous RFP expression, Tm6B is tubby larvae and Tm3 is stubby hair.

Lamka *et al.* were also able to achieve partial retraction in the *hnt* germ band by combining it with a mutant that overexpressed the insulin receptor[8]. Their conclusion was that a molecular signal related to the insulin receptor mimicked an unknown signal from the amnioserosa to the germ band that initiated retraction[8]. It is also possible that the insulin receptor overexpression in the germ band altered its mechanical properties resulting in partial retraction. The fact that only partial retraction was achieved may indicate a different mechanism of retraction than in normal germ band. The germ band must be imaged in this mutant and compared to the β-θ analysis of *hnt* and wild-type embryos to rule out a fully mechanical explanation.

Chemical Binding Analysis

It has been shown that problematic chemical binding to channel surfaces can alter cell dose in microfluidic devices. It is still unknown whether further loss of chemical occurs in the cell chamber itself, which is made of a cross-linked collagen matrix. The protocol established in Chapter 3 is generally applicable to measure chemical binding in a plethora of substrates beyond PDMS, including collagen matrix, and substrate materials used in the future fabrication of microfluidic devices.

The binding of chemical to PDMS has led to additional materials being tested as replacements for lab-on-chip devices. A comparison of potential material substitutes for PDMS is given in Table 5-1. Trade-offs must be considered when choosing the material to fabricate microfluidic devices. In order to improve upon the PDMS standard, a higher price and more difficult fabrication is necessary. Otherwise, new device configurations will need

Table 5-1: Comparison of Materials for Microfluidic Device Fabrication

Chemical Name	Cost	Ease of Prototyping	Chemical Permeability	Gas Permeability	Optically Transparent	Elasticity	Ref
PDMS	Low	Easy	High	High	Yes	Highly Elastic	[61]
texin thermoplastic polyurethane	High	Difficult	Medium	Medium	Yes	Rigid	[110]
cyclic-olefin copolymer	Low	Easy	Medium	High	Yes	Brittle	[111, 112]
polystyrene	High	Difficult	Low	Low	Yes	Stiff/Unstable at high channel aspect ratios	[113, 114]
acrylic	Low	Easy	N/A	Medium	Yes	Rigid	[115]
Styrene-ethylene-butylene-styrene	Low	Low	Low	Low	Yes	Elastic	[116]

to account for different valve and oxygenation configurations for more rigid materials.

Surface modification could also be used to change a material's molecular permeability.

However, this effect is often temporary in plasma treatments, has seen mixed results with

chemical binding, and is difficult to apply to microchannels[64].

Analysis of chemical binding can also be applied to living systems for toxicology research.

Recently, a method of removing the vitelline membrane from *Drosophila* embryos has been

outlined[117,118]. Rand *et al.* demonstrated the toxicological effects of cycloheximide, methylmercury and cytochalasin D on the developing *Drosophila* embryo[117]. The existing protocol for chemical binding can be used to investigate small molecule diffusion and quantify toxicological dose in an embryo that lacks vitelline membrane. A future application may target the developing epithelium with a chemical that interferes with internal tension in the germ band by disrupting the actin cytoskeleton. Cytochalasin D, which binds to and depolymerizes actin, was found to stall development at the end of germ band retraction[117]. Phalloidin has been found to actively bind to and stabilize actin filaments[119]; it also can be conjugated to a fluorescent dye such as Alexa Fluor 488 and is frequently used to stain actin in fixed embryos. Phalloidin and cytochalasin D are both promising candidates for mechanical perturbation and could test a combined application of chemical kinetic analysis with the ability to quantify mechanical changes with β-θ analysis. This exciting prospect works towards achieving a quantitative toxicological model that can lead to more predictive modelling. I will continue to pursue research in this direction.

REFERENCES

1   L. T. Reiter, L. Potocki, S. Chien, M. Gribskov and E. Bier, *Genome Res*, 2001, **11**, 1114–1125.

2   H. Oda and S. Tsukita, *J. Cell Sci.*, 2001, **114**, 493–501.

3   F. Schock and N. Perrimon, *Dev. Biol.*, 2002, **248**, 29–39.

4   P. Hayes and J. Solon, *Mech. Dev.*, 2017, **144**, 2–10.

5   J. A. Campos-Ortega and V. Hartenstein, *The Embryonic Development of Drosophila melanogaster*, 1985.

6   E. K. Shannon, A. Stevens, W. Edrington, Y. Zhao, A. K. Jayasinghe, A. Page-McCaw and M. S. Hutson, *Biophys. J.*, 2017, **113**, 1623–1635.

7   B. Yaiza and P. Nuria, *Dev. Dyn.*, 2011, **240**, 2379–2404.

8   M. L. Lamka and H. D. Lipshitz, *Dev. Biol.*, 1999, **214**, 102–112.

9   L. H. Frank and C. Rushlow, *Development*, **122**, 1343–1352.

10   A. Scuderi and A. Letsou, *Dev. Dyn.*, 2005, **232**, 791–800.

11   M. Lacy, Vanderbilt University, 2017.

12   H. E. Lynch, S. M. Crews, B. Rosenthal, E. Kim, R. Gish, K. Echiverri and M. S. Hutson, *Dev. Biol.*, 2013, **384**, 205–213.

13   K. L. Pope and T. J. Harris, *Development*, 2008, **135**, 2227–2238.

14   V. Hartenstein, *Atlas of Drosophila Development*, 1993.

15   O. Polyakov, B. He, M. Swan, J. W. Shaevitz, M. Kaschube and E. Wieschause, *Biophys. J.*, 2014, **107**, 998–1010.

16   R. Allena and J. J. Munoz, *Comput. Methods Biomech. Biomed. Engin.*, 2013, **16**, 235–248.

17   R. Allena, A. S. Mouronval and D. Aubry, *J. Mech. Behav. Biomed. Mater.*, 2010, **3**, 313–323.

18   G. Brodland, D. Chen and J. Veldhuis, *Int. J. Plast.*, 2006, **22**, 965–995.

19   L. Goldstein and S. Gunawardena, *J. Cell Biol.*

20   M. Koppen, *Development*, 2006, **133**, 2671–2681.

21   J. N. Jodoin, J. S. Coravos, C. Soline, C. G. Vasquez and M. Tworoger, *Dev. Cell*, 2015, **35**, 685–697.

22   D. J. DeRosier and L. G. Tilney, *Symp. Quant. Biol.*, 1982, **46**, 525–540.

23   J. M. Gomez, L. Chumakova, N. A. Bulgakova and N. H. Brown, *Nat. Commun.*, 2016, **7**, 13172.

24   T. Yeung, L. A. Georges, B. Flanagan, B. Marg, M. Ortiz, M. Funaki, N. Zahir, W. Ming, V. Weaver and P. A. Janmey, *Cell Motil. Cytoskelet.*, 2005, **60**, 24–34.

25   W. L. Murphy, T. C. McDevitt and A. J. Engler, *Nat Mater*, 2014, **13**, 547–557.

26   Z. Qin, L. Kreplak and M. J. Buehler, *PLoS One*, 2009, **4**, e7294.

27   M. Yamamoto-Hino and G. Satoshi, *Genes (Basel).*, 2013, **4**, 646–665.

28   W. T. McCleery, *Pulling Through: A Biomechanical Analysis of Normal and Aberrant Embryogenesis in Drosophila*, 2016.

29   H. J. Ray and L. Niswander, *Development*, 2012, **139**, 1701–1711.

30   M. E. Clarke and W. B. Gibbard, *Can. Child. Adolesc. Psychiatr. Rev.*, 2003, **12**, 57–63.

31   A. Delpisheh, J. Topping, M. Reyad, A. Tang and B. J. Brabin, *Eur. J. Obstet. Gynecol. Reprod. Biol.*, 2008, **138**, 49–53.

32   A. Ornoy and Z. Ergaz, *Int. J. Environ. Res. Public Heal.*, 2010, **7**, 364–379.

33   K. S. Hruska, P. A. Furth, D. B. Seifer, F. I. Sharara and J. A. Flaws, *Clin. Obs. Gyn.*, 2000, **43**, 821–829.

34   J. P. Wikswo, *Exp. Biol. Med.*, 2014, **239**, 1061–1072.

35   D. Huh, G. A. Hamilton and D. E. Ingber, *Trends Cell Biol.*, 2011, **21**, 745–754.

36   J. P. Wikswo, E. L. Curtis, Z. E. Eagleton, B. C. Evans, A. Kole, L. H. Hofmeister and W. J. Matloff, *Lab Chip*, 2013, **13**, 3496–3511.

37   D. Konar, M. Devarasetty, D. V. Yildiz, A. Atala and S. V. Murphy, *Biomed. Eng. Comput. Biol.*, 2016, **7**, 17–27.

38   K. Domansky, W. Inman, J. Serdy, A. Dash, M. H. Lim and L. G. Griffith, *Lab Chip*, 2010, **10**, 51–58.

39   S. N. Bhatia and D. E. Ingber, *Nat. Biotechnol.*, 2014, **32**, 760.

40   T. Kozlova and C. S. Thummel, *Science (80-.).*, 2003, **301**, 1911 LP-1914.

41   B. A. Edgar and P. H. O'Farrell, *Cell*, 1989, **57**, 177–187.

42   M. L. Yip, M. L. Lamka and H. D. Lipshitz, *Development*, 1997, **124**, 2129–2141.

43   J. M. Berg, *J. Biol. Chem.*, 1990, **265**, 6513–6516.

44   L. Goyal, K. McCall, J. Agapite, E. Hartwieg and H. Steller, *EMBO J.*, 2000, **19**, 589–597.

45   B. L. Baechler, C. McKnight, P. C. Pruchnicki, N. A. Biro and B. H. Reed, *Biol. Open*.

46   L. D. Deady, L. Wei and S. Jianjun, *Dev. Biol.*

47   A. Thiagalingam, A. De Bustros, M. Borges, R. Jasti, D. Compton, L. Diamond, M. Mabry and D. W. Ball, *Mol. Cell Biol.*, 1996, **16**, 5335–5345.

48   K. Bambardekar, R. Clément, O. Blanc, C. Chardès and P.-F. Lenne, *Proc. Natl. Acad. Sci.*, 2015, **112**, 1416 LP-1421.

49   M. Morimatsu, A. H. Mekhdjian, A. S. Adhikari and A. R. Dunn, *Nano Lett.*, 2013, **13**, 3985–3989.

50   N. Borghi, M. Sorokina, O. G. Shcherbakova, W. I. Weis, B. L. Pruitt, W. J. Nelson and A. R. Dunn, *Proc. Natl. Acad. Sci. U. S. A.*, 2012, **109**, 12568–12573.

51   Y. Zhang, F. Wei, Y.-C. Poh, Q. Jia, J. Chen, J. Chen, J. Luo, W. Yao, W. Zhou, W. Huang, F. Yang, Y. Zhang and N. Wang, *Nat. Protoc.*, 2017, **12**, 1437.

52   G. W. Brodland, V. Conte, P. G. Cranston, J. Veldhuis, S. Narasimhan, M. S. Hutson, A. Jacinto, F. Ulrich, B. Baum and M. Miodownik, *Proc. Natl. Acad. Sci.*, 2010, **107**, 22111 LP-22116.

53   G. W. Brodland, J. H. Veldhuis, S. Kim, M. Perrone, D. Mashburn and M. S. Hutson, *PLoS One*.

54   F. Schock, *Genes Dev.*, 2003, **17**, 597–602.

55   S. M. Crews, W. T. McCleery and M. S. Hutson, *Dev. Dyn.*, 2015, **245**, 402–413.

56   J. Schindelin, I. Arganda-Carreras, E. Frise, V. Kaynig, M. Longair and T. Pietzsch, *Nat.*

Methods, 2012, **9**, 676–682.

57   D. N. Mashburn, H. E. Lynch, X. Ma and M. S. Hutson, *Cytometry*, 2012, **81**, 409–418.

58   D. P. Kiehart, C. G. Galbraith, K. A. Edwards, W. L. Rickoll and R. A. Montague, *J. Cell Biol.*, 2000, **149**, 471–490.

59   Z. Sun, C. Amourda, M. Shagirov, Y. Hara, T. E. Saunders and Y. Toyama, *Nat. Cell Biol.*, 2017, **19**, 375.

60   K. Saadin, J. M. Burke, N. P. Patel, R. E. Zubajlo and I. M. White, *Microdevices*, 2013, **15**, 645–655.

61   B. H. Jo, L. M. Van Lerberghe, K. M. Motsegood and D. J. Beebe, *J. Microeletromech. Syst.*, 2009, **9**, 76–81.

62   M. W. Toepke and D. J. Beebe, *Lab Chip*, 2006, **6**, 1484–1486.

63   J. D. Wang, N. J. Douville, S. Takayama and M. ElSayed, *Ann. Biomed. Eng.*, 2012, **40**, 1862–1873.

64   B. J. van Meer, H. de Vries, K. S. A. Firth, J. van Weerd, G. J. Tertoolen, H. B. J. Karperien, P. Jonkheijm, C. Denning, A. P. Ijzerman and C. L. Mummery, *Biochem. Biophys. Res. Commun.*, 2017, **482**, 323–328.

65   M. T. Martin, T. B. Knudsen, D. M. Reif, K. A. Houck, R. S. Judson, R. J. Kavlock and D. J. Dix, *Biol. Reprod.*, 2011, **85**, 327–339.

66   J. E. Klaunig, M. A. Babich, K. P. Baetcke, J. C. Cook, J. C. Corton, R. M. David, J. G. DeLuca, D. Y. Lai, R. H. McKee, J. M. Peters, R. A. Roberts and P. A. Fenner-Crisp, *Crit. Rev. Toxicol.*, 2003, **33**, 655–780.

67   H. N. D. and F. P. A., *J. Appl. Toxicol.*, 2011, **33**, 265–272.

68   C. Lau, J. R. Thibodeaux, R. G. Hanson, M. G. Narotsky, J. M. Rogers, A. B. Lindstrom and E. Al., *Toxicol. Sci.*, 2006, **90**, 508–510.

69   C. Yang, Y. S. Tan, J. R. Harkema and S. Z. Haslam, *Reprod. Toxicol.*, 2009, **27**, 299—306.

70   M. B. Macon, L. R. Villanueva, K. Tatum-Gibbs, R. D. Zehr, M. J. Strynar, J. P. Stanko, S. S. White, L. Helfant and S. E. Fenton, *Toxicol. Sci.*, 2011, **122**, 134–145.

71   D. Dixon, C. E. Reed, A. B. Moore, E. A. Gibbs-Flournoy, E. P. Hines, E. A. Wallace, J. P. Stanko, Y. Lu, W. N. Jefferson, R. R. Newbold and S. E. Fenton, *Reprod. Toxicol.*, 2012, **33**, 506–512.

72   L. B. Biegel, R. C. Liu, M. E. Hurtt and J. C. Cook, *Toxicol. Appl. Pharmacol.*, 1995, **134**, 18–25.

73   C. M. Markey, E. H. Luque, M. Munoz De Toro, C. Sonnenschein and A. M. Soto, *Biol. Reprod.*, 2001, **65**, 1215–1223.

74   L. N. Vandenberg, M. V. Maffini, C. M. Schaeberle, A. A. Ucci, C. Sonnenschein, B. S. Rubit and E. Al., *Reprod. Toxicol.*, 2008, **26**, 209–210.

75   P. Bhattacharya and A. F. Keating, *Toxicol. Appl. Pharmacol.*, 2012, **261**, 227–235.

76   N. Quignot, M. Arnaud, F. Robidel, A. Lecomte, M. Tournier, C. Cren-Olive and R. Barouki, *Reprod. Toxicol.*, 2012, **33**, 339–352.

77   C. A. Richter, L. S. Birnbaum, F. Farabollini, R. R. Newbold, B. S. Rubin, C. E. Talsness, J. G. Vandenbergh, D. R. Walser-Kuntz and F. S. vom Saal, *Reprod. Toxicol.*, 2007, **24**, 199–224.

78   M. Munoz-de-Toro, C. M. Markey, P. R. Wadia, E. H. Luque, B. S. Rubin, C. Sonnenschein and A. M. Soto, *Endocrinology*, 2005, **146**, 4138–4147.

79   A. P. Tharp, M. V Maffini, P. A. Hunt, C. A. VandeVoort, C. Sonnenschein and A. M. Soto, *Proc. Natl. Acad. Sci.*, 2012, **109**, 8190 LP-8195.

80   S. Jenkins, N. Raghuraman, I. Eltoum, M. Carpenter, J. Russo and C. A. Lamartiniere, *Environ. Heal. Perspect.*, 2009, **117**, 910–915.

81   A. M. Betancourt, I. A. Eltoum, R. A. Desmond, J. Russo and C. A. Lamartiniere, *Environ. Health Perspect.*, 2010, **118**, 1614–1619.

82   L. Hilakivi-Clarke, *Breast Cancer Res*, 2014, **16**, 208.

83   R.-J. Pei, M. Sato, T. Yuri, N. Danbara, Y. Nikaido and A. Tsubura, *In Vivo*, 2003, **17**, 349—357.

84   T. G. Whitsett and C. A. Lamartiniere, *Expert Rev. Anticancer Ther.*, 2006, **6**, 1699–1706.

85   W. A. Fritz, L. Coward, J. Wang and C. A. Lamartiniere, *Carcinogenesis*, 1998, **19**, 2151–2158.

86   C. A. Lamartiniere, *J. Mammary Gland Biol. Neoplasia*, 2002, **7**, 67–76.

87   J. C. L. Tou and L. U. Thompson, *Carcinogenesis*, 1999, **20**, 1831–1835.

88   V. Dieras, *Oncology*, 1997, **11**, 31–33.

89   Comptox.epa.gov, EPA Chemical Database.

90   W. T. Jewell, R. A. Hess and M. G. Miller, *Toxicol. Appl. Pharmacol.*, 1998, **149**, 159–166.

91   W. Zhu, Z. Dang, J. Qiu, C. Lv, G. Jia, L. Li and Z. Zhou, *Chirality*, 2007, **19**, 632–637.

92   V. S. Shirure and S. C. George, *Lab Chip*, 2017, **17**, 681.

93   Www.t3db.ca, Toxin Exposome Database.

94   Http://sitem.herts.ac.uk/aeru/ppdb/en, Pesticide Properties Database.

95   J. A. Rothwell, A. J. Day and M. R. A. Morgan, *J. Agric. Food Chem.*, 2005, **53**, 4355–4360.

96   X. Gao and J. Chorover, *Environ. Chem.*, 2012, **9**, 148–157.

97   T. M. Squires, R. J. Messinger and S. R. Manalis, *Nat. Biotechnol.*, 2008, **26**, 417–426.

98   T. Gervais and K. F. Jensen, *Chem. Eng. Sci.*, 2006, **61**, 1102–1121.

99   G. Byron, C. Daniel, H. Xiaoyi, P. A. R. and W. Carla, *J. Mol. Recognit.*, 1999, **12**, 293–299.

100   A. Lionello, J. Josserand, H. Jensen and H. H. Girault, .

101   R. A. Vijayendran, F. S. Ligler and D. E. Leckband, *Anal. Chem.*, 1999, **71**, 5405–5412.

102   J. D. Plessis, W. J. Pugh, A. Judefeind and J. Hadgraft, *Eur. J. Pharm. Sci*, 2002, **15**, 63–69.

103   E. L. DiFilippo and R. P. Eganhouse, *Environ. Sci. Technol.*, 2010, **44**, 6917–6925.

104   E. Baltussen, P. Sandra, F. David and C. Cramers, *J. Microcolumn Sep.*, 1999, **11**, 737–747.

105   M. Milosevic, *Internal Reflection and ATR Spectroscopy*, 2012.

106   S. G. Kuntz and M. B. Eisen, *PLoS Genet.*

107   L. C. Butler, G. B. Blanchard, A. J. Kabla, N. J. Lawrence, D. P. Welchman, L. Mahadevan, R. J. Adams and B. Sanson, *Nat. Cell Biol.*, 2009, **11**, 859+.

108   C. Collinet, M. Rauzi, P.-F. Lenne and T. Lecuit, *Nat. Cell Biol.*, 2015, **17**, 1247.

109   D. Kong, F. Wolf and J. Großhans, *Mech. Dev.*, 2017, **144**, 11–22.

110   W. I. Wu, K. N. Sask, J. L. Brash and P. R. Selvaganapathy, *Lab Chip*, 2012, **12**, 960–970.

111   G. Khanarian, *Opt. Eng.*, 2001, **40**, 40–46.

112   L. Chen, Y. Yang, H. G. Craighead and K. H. Lee, *Electrophoresis*, 2005, **26**, 1800–1806.

113   S. Halldorsson, E. Lucumi, R. Gomez-Sjoberg and R. M. T. Fleming, *Biosens. Bioelectron.*, 2015, **63**, 218–231.

114   P. N. Nge, C. I. Rogers and A. T. Woolley, *Chem. Rev.*, 2013, **113**, 2550–2583.

115   W. Zhang, S. Lin, C. Wang, J. Hu, C. Li, Z. Zhuang, Y. Zhou, R. A. Mathies and C. J. Yang, *Lab Chip*, 2009, **9**, 3088–3094.

116   K. Domansky, J. D. Sliz, N. Wen, C. Hinojosa, G. Thompson and J. P. Fraser, *Microfluid. Nanofluidics*.

117   M. D. Rand, A. L. Kearney and T. Clason, *Insect Biochem. Mol. Biol.*, 2010, **40**, 792–804.

118   M. D. Rand, *J. Vis. Exp.*

119   R. E. Mahaffy and T. D. Pollard, *Biochemistry*, 2008, **47**, 6460–6467.